UCLA
UCLA Electronic Theses and Dissertations

Title

Magnetic Field Based Quasistatic Indoor Position Sensing and Navigation: Enhancing Precision Tracking and Location Accuracy for First Responders in Emergency Situations

Permalink

https://escholarship.org/uc/item/8h86d36w

Author

Wilson, Tristan Alexander

Publication Date

2024

Peer reviewed|Thesis/dissertation

eScholarship.org Powered by the California Digital Library
University of California

UNIVERSITY OF CALIFORNIA
Los Angeles

Magnetic Field Based Quasistatic Indoor Position Sensing and Navigation: Enhancing Precision Tracking and Location Accuracy for First Responders in Emergency Situations

A thesis submitted in partial satisfaction
of the requirements for the degree
Master of Science in Electrical and Computer Engineering

by

Tristan Alexander Wilson

2024

© Copyright by
Tristan Alexander Wilson
2024

ABSTRACT OF THE THESIS

Magnetic Field Based Quasistatic Indoor Position Sensing and Navigation: Enhancing Precision Tracking and Location Accuracy for First Responders in Emergency Situations

by

Tristan Alexander Wilson
Master of Science in Electrical and Computer Engineering
University of California, Los Angeles, 2024
Professor Yuanxun Wang, Chair

First responders navigating compromised environments, such as burning buildings, often face obstructed fields of view, making navigation challenging. Alleviating these difficulties is crucial for providing essential aid to individuals at risk. Quasistatic electromagnetics serve as an effective tool for real-time position sensing and tracking within non-line-of-sight, steel-reinforced structures. The quasistatic regime is characterized by electromagnetic waves that vary slowly over time, allowing for deep penetration into structures with minimal signal loss. We propose a multiaxial system architecture that couples magnetoquasistatic and electroquasistatic waves radiating from collocated loop antennas and piezoelectric field emitters. Our research into the radiation characteristics of these devices revealed that piezoelectric emitters cannot produce fields strong enough for effective coverage in single-story buildings. Consequently, we adjusted to a magnetoquasistatic sensor fusion system which predicts positioning with meter-level accuracy. The efficacy and accuracy of our system operating within a single-story structure were verified and presented in a live demonstration.

The thesis of Tristan Alexander Wilson is approved.

Ian Roberts

Aydin Babakhani

Yuanxun Wang, Committee Chair

University of California, Los Angeles

2024

To Professor Tavakoli ...

for guiding me toward the brightest light of engineering.

TABLE OF CONTENTS

1 Introduction **1**

1.1 Background and Motivation 1

1.2 Quasistatic Electromagnetic Theory 3

1.3 Piezoelectric Theory 4

1.4 Structure of the Thesis 7

2 High Voltage Drive Studies on 47 kHz Lithium Niobate Transmitters . **9**

2.1 Introduction 9

2.2 Length Extensional Resonance and Transmitter Analysis 11

2.3 High Voltage Experiment 14

2.4 Results 15

2.5 Conclusion 16

3 Electric Field Pattern Measurements of 82 kHz Lithium Niobate Transmitters **17**

3.1 Introduction 17

3.2 Principle of Operation and Simulations 18

3.2.1 Electric Field Distribution, Simulation, and Analysis 19

3.3 Near Field Pattern Measurements 23

3.4 Conclusion 25

4 Pushing Acoustically-Driven Transmitters to the MHz Regime **26**

4.1 Introduction 26

4.2 Method of Operation 28

4.3 Resonant Transducer Analysis 31
4.4 Near Field Transmission Measurements 34
4.5 Radiation Efficiency Estimation 36
4.6 Conclusion 38

5 Transition to Quasistatic Magnetic Field Positioning 39
5.1 Introduction 39
5.2 Piezoelectric Transmitter Range Limitations 40
5.3 Broadband Magnetic Field Sweeps and Frequency Selection 42
5.4 Conclusion 45

6 Quasistatic Magnetic Field Positioning in Single-Story Steel-Reinforced Building 47
6.1 Introduction 47
6.2 Multiaxial System Architecture and Hardware Development 47
6.3 System Integration and Sensor Fusion 53
6.4 Live Position-Sensing Demonstration and Results 57
6.5 Conclusion 60

7 Conclusion and Future Work 61
7.1 Recapitulation of Key Findings 61
7.2 Extension of Piezoelectric Transmitter Operation 62
7.2.1 Direct Antenna Modulation 63
7.2.2 Piezoelectric Transmitter Arraying 63
7.3 MQS System Scaling 64
7.3.1 Positioning in Multi-Story Steel-Reinforced Structures 64
7.3.2 Miniaturization of System Hardware 64

References **66**

LIST OF FIGURES

2.1 Transmitter constructed with lithium niobate rod and copper toroids. 10

2.2 Schematic of $LiNbO_3$ transmitter with complex circuit model representing the piezoelectric material. 12

2.3 Impedance spectrum of $LiNbO_3$ transmitter. 13

2.4 Block diagram of high voltage experimental setup. 14

2.5 Received electric field magnitude as a function of input voltage. 15

3.1 Schematic of the measurement setup. 19

3.2 Acoustically driven mechtenna constructed with lithium niobate rod and aluminum field-shaping toroids. 20

3.3 FEKO simulation setup (left) and results (right). 21

3.4 Electric field distributions between parallel plates. Boxes show 1k, 5k, 10k ppm areas. (a) $d/W = 0.5$, (b) $d/W = 0.8$ and (c) $d/W = 1$ 22

3.5 Trade-space showing size/separation of plates vs ROI for 3 homogeneity levels . 23

3.6 Experimental setup showing DUT mounted on turntable along the direction of the Electric field. 24

3.7 Normalized power pattern for DUT operating at resonance. Arrows at the center indicate rotating dipole moment of DUT. Parallel lines show alternating electric field between the plates captured at $t = 0$ 25

4.1 Size of the MARSIS sounding radar antenna (horizontal line) compared to the spacecraft and a human silhouette. 27

4.2 Wiring configuration diagram of $LiNbO_3$ transmitter. 29

4.3 Lithium niobate piezoelectric transmitter with 3D-printed toroidal radiating mechanisms. 29

4.4 Lithium niobate crystals resonant at 1 MHz in fully-plated electrode configuration (left) and ring electrode configuration (right). 31
4.5 Complex circuit model for piezoelectric resonators [1]. 32
4.6 Impedance spectra at resonance of lithium niobate transmitter (a) with fully-plated crystal and (b) with ring electrode crystal. 34
4.7 Block diagram of the electric field drop-off experimental setup. 34
4.8 Experimental setup for electric field drop-off measurements, depicting the positioning of the transmitter and EQS probe. 35
4.9 Comparison of electric field from fully-plated transmitter and ring electrode transmitter in an outdoor line-of-sight environment. 36

5.1 Experimental setup for 82 kHz $LiNbO_3$ transmitter field decay measurements. . 40
5.2 Near field drop-off of 82 kHz $LiNbO_3$ transmitter compared to exponential decay model. 42
5.3 Block diagram of single-axis MQS system. 43
5.4 Setup of transmitter and receiver for broadband measurements. 44
5.5 Received power density drop-off as a function of frequency at four discrete distances from transmitter. 45

6.1 Block diagram of multiaxial MQS transmitter. 48
6.2 Development of multiaxial transmitter electronics and antenna. 49
6.3 Impedance spectra of transmitter loop antenna axes at resonance. 50
6.4 Block diagram of multiaxial MQS receiver. 51
6.5 Development of multiaxial receiver electronics and antenna. 51
6.6 Impedance spectra of receiver loop antenna axes at resonance. 53
6.7 Mobile receiver unit used for real-time position sensing. 54
6.8 Comparison of measured positioning data with theoretical model. 56

6.9 Mobile transmitter unit placed outside of building generating magnetic fields at 3 MHz for position-sensing. 57

6.10 Mobile receiver unit being used to perform real-time prediction of individual in steel-reinforced structure. 58

6.11 Position-sensing demo screen showing received magnetic field power, live video feed, and positioning prediction with calculated errors. 59

LIST OF TABLES

1.1 Typical material properties of lithium niobate [2]. 6

2.1 Complex circuit model parameters 11

2.2 Material constants determined from Smits' method for $LiNbO_3$ resonator in parallel with stray capacitance and toroid capacitance 13

3.1 Selected values of ROI Area for different d/W values and homogeneity levels . . 22

4.1 Complex circuit model component values derived from material coefficients using Smits' method [3, 4], and from geometry and equations provided by Sherrit et al. [1]. 33

4.2 Calculated radiation efficiency values at 1 MHz. 37

5.1 Best fit parameters describing 82 kHz $LiNbO_3$ transmitter field decay in steel-reinforced structure. 42

6.1 Natural resonant frequency of each transmitter loop antenna axis. 50

6.2 Loop diameter of each axis of multiaxial receiver antenna. 52

6.3 Natural resonant frequency of each receiver loop antenna axis. 52

LIST OF ACRONYMS

POINTER - Precision Outdoor and Indoor Navigation and Tracking for Emergency Responders 1

MQS - Magnetoquasistatic 1

EQS - Electroquasistatic 2

M/EQS - Magnetoelectroquasistatic 2

LoS - Line-of-Sight 2

NLoS - Non-Line-of-Sight 2

ESA - Electrically Small Antenna 9

LF - Low Frequency 9

VLF - Very Low Frequency 9

$LiNbO_3$ - Lithium Niobate 9

$LiNbO_3$ - Lithium Niobate 10

LE - Length Extensional Resonance 11

AWG - Arbitrary Waveform Generator 14

PA - Power Amplifier 14

ADC - Analog-to-Digital Converter 14

DSP - Digital Signal Processing 14

DUT - Device Under Test 18

DAQ - Data Acquisition System 18

MARSIS - Mars Advanced Radar for Subsurface and Ionospheric Sounding 26

GPR - Ground Penetrating Radar 27

RSA - Real-Time Spectrum Analyzer 34

CW - Continuous Wave 35

VA - Voltage Amplifier 35

RFSG - RF Signal Generator 43

LNA - Low Noise Amplifier 43

SNR - Signal-to-Noise Ratio 47

ABS - Acrylonitrile Butadiene Styrene 49

GNSS - Global Navigation Satellite System 55

GUI - Graphical User Interface 55

HF - High Frequency 61

DAM - Direct Antenna Modulation 63

ACKNOWLEDGMENTS

This research was carried out at the Jet Propulsion Laboratory, California Institute of Technology, and was sponsored by the JPL Year-Round Internship Program and the National Aeronautics and Space Administration (80NM0018D0004).

Chapter Two is a version of the paper, "High Drive Voltage Studies on Lithium Niobate Length Extensional Resonators and Their Generated Quasistatic Electric Fields," co-authored with S. Sherrit, S. P. M. Nagaraja, B. Feyissa, D. Willey, and D. D. Arumugam, and published in the 2023 IEEE International Ultrasonics Symposium proceedings. S. Sherrit helped with determining piezoelectric material parameters from $LiNbO_3$ impedance measurements, S. P. M. Nagaraja provided guidance and assisted in data collection, B. Feyissa provided data processing code, D. Willey assisted with material presentation, and D. D. Arumugam was the PI. The paper is available online at DOI: 10.1109/IUS51837.2023.10307273. This work was funded by the Department of Homeland Security Science and Technology Directorate.

Chapter Three is a version of the paper, "Electric Field Pattern Measurements of Acoustically Driven Piezoelectric Field Emitters," co-authored with S. P. M. Nagaraja, B. Feyissa, J. Bush, and D. D. Arumugam, and published in the 2023 Antenna Measurement Techniques Association Symposium proceedings. S. P. M. Nagaraja organized the material presentation, B. Feyissa simulated the parallel plate electric field response, and D. D. Arumugam was the PI. The paper is available online at DOI: 10.23919/AMTA58553.2023.10293717. This work was funded by the Department of Homeland Security Science and Technology Directorate.

Chapter Four is a version of the paper, "Pushing Piezoelectric Transmitters to the MHz Regime," co-authored with S. P. M. Nagaraja, S. Sherrit, A. Wildanger, and D. D. Arumugam, and is in preparation for publication. S. P. M. Nagaraja provided guidance and assisted with efficiency determination, S. Sherrit verified the piezoelectric analysis, A. Wildanger designed the $LiNbO_3$ crystal holders, and D. D. Arumugam was the PI. This work was funded by the JPL Blue Sky Studies Program.

I would like to thank Stewart Sherrit, Brook Feyissa, Junhee Park, Dean Wright, Jeffrey

Burton, Jack Bush, Lucy Martinez, Nithin Martin Sundar, Adam Wildanger, Talar Yessayan, Sebastian Davis, and Devin Willey. I would also like to thank Prof. Ian Roberts, Prof. Aydin Babakhani, and Prof. Ethan Wang for serving on my master's thesis committee. Finally, I would like to thank my mentors Darmindra Arumugam and Srinivas Prasad Mysore Nagaraja for providing tireless guidance and teaching me everything that they know.

CHAPTER 1

Introduction

1.1 Background and Motivation

POINTER (Precision Outdoor and Indoor Navigation and Tracking for Emergency Responders) is a project developed by NASA's Jet Propulsion Laboratory for the Department of Homeland Security's Science and Technology Directorate [5]. This project seeks to provide accurate and reliable position-sensing and location accuracy for first responders navigating compromised environments. First responders frequently enter environments in which their fields-of-view are obstructed by smoke, fire, and other obstacles. In these situations, it is necessary for someone to be outside the structure that is monitoring the movement and position of the first responder, providing in-ear navigation instructions when necessary. The context provided to fire chiefs and other commanding individuals is critical in high pressure emergency situations.

To have a reliable position-sensing system in these critical environments, it is often not ideal to utilize radio waves that are highly susceptible to field perturbations and attenuation from obstacles in a non-line-of-sight environment. What makes the POINTER system unique is that position-sensing is performed with magnetic fields radiating in the quasistatic regime, also known as magnetoquasistatic (MQS) waves. This regime is typically characterized by operating frequencies below 1 MHz, in which the wavelengths can be from a few meters to a few thousand meters [6]. At these frequencies, the wavelength is massive compared to physical objects. Because of this, the waves appear to be nearly stationary, appearing quite similar to static magnetic fields with respect to neighboring objects. This ensures that interference and perturbation to the waves from the surrounding objects are minimal,

allowing the waves to pass through objects quite easily.

One version of the POINTER system was developed and demonstrated to work in a two-story residential structure in 2021 [7]. The system architecture consisted of several transmitters placed on telescoping masts attached to a fire truck. These transmitters generated MQS fields at 80 kHz which were then received by cell phone-sized units that detect the signal, calculate position based on inversion algorithms, then transmit the location to a user base station that displays position in real-time on a graphical user interface. This iteration of POINTER worked quite effectively in residential structures, however it was also found that MQS fields at 80 kHz failed to penetrate far enough into steel-reinforced structures to provide reliable position-sensing.

To improve the POINTER system, it was proposed to combine MQS fields with electroquasistatic (EQS) field radiation, resulting in magnetoelectroquasistatic (M/EQS) fields. This form of electromagnetic field generation occurs based on the collocation of EQS and MQS generators, resulting in improved structure penetration. One effort proposed to generate EQS fields with a counter-wound normal-mode helical antenna, which creates opposing circular currents that cancel out magnetic fields [8]. This results in EQS radiation with a dipole-like field pattern. These antennas were found to operate well in a single-axis configuration, but extending to triaxial transmission resulted in significant axial coupling that heavily distorted the radiation pattern, making operation highly unpredictable. Due to this unpredictability, it was necessary to pursue the development of a new technology to generate EQS fields.

This work extends the previous version of POINTER and investigates the potential use of using piezoelectric transmitters as generators of EQS fields by developing prototypes resonant at different frequencies, observing their high voltage handling capabilities, measuring their electric field patterns, and analyzing their electric field drop-off in both line-of-sight (LoS) and non-line-of-sight (NLoS) environments. Next, we move to a brief discussion of the preliminary electromagnetic and piezoelectric theory, then provide an explanation of the structure of this thesis.

1.2 Quasistatic Electromagnetic Theory

Maxwell's equations provide a general framework for understanding the dynamics of electric and magnetic fields. However, in many practical situations, such as low-frequency applications or where changes occur over long periods of time, a quasistatic approximation is sufficient and simplifies electromagnetic analysis significantly [9]. The full Maxwell's equations in differential form are:

$$\nabla \times \mathbf{E} = -\frac{\partial \mathbf{B}}{\partial t} \quad \text{(Faraday's law of induction)} \tag{1.1}$$

$$\nabla \times \mathbf{H} = \mathbf{J} + \frac{\partial \mathbf{D}}{\partial t} \quad \text{(Ampère's law with Maxwell's addition)} \tag{1.2}$$

$$\nabla \cdot \mathbf{D} = \rho \quad \text{(Gauss's law for electricity)} \tag{1.3}$$

$$\nabla \cdot \mathbf{B} = 0 \quad \text{(Gauss's law for magnetism)} \tag{1.4}$$

where $\mathbf{E}$ is the electric field, $\mathbf{B}$ is the magnetic flux density, $\mathbf{H}$ is the magnetic field, $\mathbf{D}$ is the electric displacement field, $\mathbf{J}$ is the current density, and ρ is the charge density.

In the quasistatic regime, we assume that the changes in fields and charges occur so slowly that the propagation effects of electromagnetic waves can be neglected. This leads to two main approximations. The first is that under EQS conditions, the magnetic induction term $\frac{\partial \mathbf{B}}{\partial t}$ in Faraday's law can be neglected. This is applicable when the changes in the electric field are sufficiently slow. That is,

$$\nabla \times \mathbf{E} \approx 0 \tag{1.5}$$

Consequently, Faraday's law simplifies, and the electric field can be approximated as being electrostatic, though still driven by slowly varying charges and potentials. Under EQS conditions, Maxwell's equations reduce to:

$$\nabla \times \mathbf{E} \approx 0 \tag{1.6}$$

$$\nabla \times \mathbf{H} = \mathbf{J} + \frac{\partial \mathbf{D}}{\partial t} \tag{1.7}$$

$$\nabla \cdot \mathbf{D} = \rho \tag{1.8}$$

$$\nabla \cdot \mathbf{B} = 0 \tag{1.9}$$

The second approximation is that under MQS conditions, the displacement current term $\frac{\partial \mathbf{D}}{\partial t}$ in Ampère's law is negligible. This approximation is valid when currents change slowly, such that

$$\nabla \times \mathbf{H} \approx \mathbf{J} \tag{1.10}$$

This simplification implies that the magnetic fields behave almost like magnetostatic fields, influenced by steady currents. Under MQS conditions, Maxwell's equations reduce to:

$$\nabla \times \mathbf{E} = -\frac{\partial \mathbf{B}}{\partial t} \tag{1.11}$$

$$\nabla \times \mathbf{H} \approx \mathbf{J} \tag{1.12}$$

$$\nabla \cdot \mathbf{D} = \rho \tag{1.13}$$

$$\nabla \cdot \mathbf{B} = 0 \tag{1.14}$$

These approximations greatly simplify the complexities of Maxwell's equations and are adequate in describing the propagation of quasistatic fields for position-sensing applications.

1.3 Piezoelectric Theory

Next, we move forward with a brief discussion of the fundamental theory of piezoelectric crystals. The fundamental constitutive equations for piezoelectric materials relate the electric field, electric displacement, mechanical stress, and strain [2, 10, 11] are

$$D_i = \epsilon_{ij} E_j + d_{ijk} T_k \tag{1.15}$$

$$S_i = s_{ijkl} T_{kl} + d_{kij} E_j \tag{1.16}$$

where D_i is the electric displacement, E_j is the electric field, T_k is the mechanical stress, S_i is the mechanical strain, ϵ_{ij} is the permittivity, s_{ijkl} is the compliance tensor at constant electric field, and d_{ijk} is the piezoelectric stress coefficient. This matrix can vary based on the crystal symmetry and orientation, but a general form for a piezoelectric material is given to be

$$\begin{bmatrix} D_1 \\ D_2 \\ D_3 \end{bmatrix} = \begin{bmatrix} d_{11} & d_{12} & d_{13} \\ d_{21} & d_{22} & d_{23} \\ d_{31} & d_{32} & d_{33} \end{bmatrix} \begin{bmatrix} T_1 \\ T_2 \\ T_3 \end{bmatrix} + \begin{bmatrix} \epsilon_{11} & 0 & 0 \\ 0 & \epsilon_{22} & 0 \\ 0 & 0 & \epsilon_{33} \end{bmatrix} \begin{bmatrix} E_1 \\ E_2 \\ E_3 \end{bmatrix} \tag{1.17}$$

and the relations between stress and strain in the presence of an electric field are given by

$$\begin{bmatrix} S_1 \\ S_2 \\ S_3 \end{bmatrix} = \begin{bmatrix} s_{11} & s_{12} & s_{13} \\ s_{21} & s_{22} & s_{23} \\ s_{31} & s_{32} & s_{33} \end{bmatrix} \begin{bmatrix} T_1 \\ T_2 \\ T_3 \end{bmatrix} + \begin{bmatrix} d_{11} & d_{12} & d_{13} \\ d_{21} & d_{22} & d_{23} \\ d_{31} & d_{32} & d_{33} \end{bmatrix} \begin{bmatrix} E_1 \\ E_2 \\ E_3 \end{bmatrix} \tag{1.18}$$

Since the majority of our piezoelectric focus is related to the longitudinal (length-extensional) mode of resonance, we wish to understand this mode. The resonance frequency for the longitudinal mode in a piezoelectric rod can be expressed as

$$f_{\mathrm{s}} = \frac{n}{2L} \sqrt{\frac{E}{\rho}} \tag{1.19}$$

where f_{s} is the resonance frequency, n is the mode number , L is the length of the piezoelectric rod, E is the Young's modulus, and ρ is the density of the material. Another important parameter is the mechanical quality factor, which indicates the energy dissipation characteristics of the piezoelectric material, and is given by

Table 1.1: Typical material properties of lithium niobate [2].

Property	Symbol	Value
Relative Dielectric Constant (Parallel)	$\epsilon_{33}^{T}/\epsilon_0$	30
Relative Dielectric Constant (Perpendicular)	$\epsilon_{11}^{T}/\epsilon_0$	84
Piezoelectric Stress Constant (Longitudinal)	d_{33}	6 pC/N
Piezoelectric Stress Constant (Transverse)	d_{31}	-1 pC/N
Elastic Stiffness at Constant Electric Field (C-axis)	c_{33}^{E}	2.45 $\times 10^{11}$ N/m^2
Elastic Stiffness at Constant Electric Field (A-axis)	c_{11}^{E}	2.03 $\times 10^{11}$ N/m^2
Curie Temperature	T_C	1210 °C

$$Q_m = \frac{\pi f_{\mathrm{s}} L^2}{\eta v} \tag{1.20}$$

where η is the mechanical damping coefficient, and v is the speed of sound in the crystal. There is also the electrical quality factor, which related to the electrical losses and can be calculated using

$$Q_e = \frac{1}{\omega C R} \tag{1.21}$$

where $\omega = 2\pi f_{\mathrm{s}}$ is the angular frequency, C is the capacitance of the piezoelectric element, and R is the electrical resistance. We also include the impedance at resonance, which can be approximated as:

$$Z_{\mathrm{res}} = R + j\left(\omega L - \frac{1}{\omega C}\right) \tag{1.22}$$

where R is the resistance, L is the inductance, C is the capacitance, and j is the imaginary unit.

1.4 Structure of the Thesis

Following an overview of the project, previous work done, and essential theoretical principles, we now give a breakdown of the research performed for this thesis. The initial goal for this research was to develop a multiaxial M/EQS system constructed with collocated EQS and MQS generators, each of which having three axes. The initial goal was to utilize piezoelectric transmitters acting as EQS generators and loop antennas acting as MQS generators, both of which operating around 80 kHz. The research performed for this thesis can be categorized into two tracks: efforts related to the development and study of piezoelectric transmitters for quasistatic position sensing and other radar applications, and efforts related to the development of a MQS sensor fusion position-sensing system.

Investigation into the radiation characteristics of lithium niobate piezoelectric transmitters is the main focus of Chapters 2 through 5. Chapter 2 of this work studies piezoelectric charge generators operating at 47 kHz and how they respond to high voltage excitation signals. Chapter 3 extends the study of piezoelectric transmitters to 82 kHz and presents a novel method of obtaining near field pattern measurements at these low frequencies. Chapter 4 extends even further to piezoelectric transmitters operating at 1 MHz by analyzing their radiation performance in an outdoor LoS environment, and comparing the efficiency of these devices to similarly sized electrically small dipoles operating at the same frequency. This section of the thesis also discusses some other applications of these devices, such as spacecraft radar hardware.

The next stage of the work begins with Chapter 5. This section presents results from an indoor experiment with piezoelectric transmitters generating EQS fields into a steel-reinforced building, indicating that these devices are not conducive for deep penetration into these structures. From here, the decision to switch to a system comprised of only MQS generators was made, and broadband measurements were performed indoors to determine the optimal operating frequency for deep penetration and acceptable signal-to-noise ratio. Chapter 6 presents the design of a multiaxial MQS position-sensing system along with the development of transmitter and receiver hardware. This design culminated in a live demon-

stration of accurate position-sensing in a steel-reinforced structure for the Department of Homeland Security, and details are presented. Chapter 7 discusses the results obtained through this research, and presents a discussion of future work to be done to enhance the development of both piezoelectric transmitters and MQS position-sensing systems.

CHAPTER 2

High Voltage Drive Studies on 47 kHz Lithium Niobate Transmitters

2.1 Introduction

Transmitters operating in the Low Frequency (LF) and Very Low Frequency (VLF) bands are limited to direct line-of-sight communications and typically require large antennas due to the wavelengths of these signals being large in these frequency ranges. For applications that require a compact form-factor, however, it is necessary to utilize Electrically Small Antennas (ESAs). The downsides of ESAs in these bands are that they are still quite large, radiate with very low efficiency [12], and are limited in both quality factor and bandwidth [13]. It has been found that utilizing alternative forms of electromagnetic radiating mechanisms allows for greater radiation efficiency in a smaller form-factor [14]. Mechanical antennas are promising alternatives to traditional antennas in transmitting and receiving systems due to their ability to radiate at low frequencies with high mechanical Q-factors [12,15]. Perhaps one of the most interesting subsets of mechanical antennas, or 'mechtennas', are those that utilize piezoelectric crystals. These devices generate electrical charge via mechanical oscillations due to the piezoelectric effect [14, 16].

This research studies the performance of an acoustically-driven mechtenna that is constructed with a Lithium Niobate ($LiNbO_3$) crystal that has a quasi-longitudinal resonance mode around 47 kHz. This cylindrical crystal rod is fabricated to have a 36° rotated Y-cut orientation, and has a length of 7 cm and a diameter of 2 cm. In addition to the $LiNbO_3$ rod, the transmitter is constructed with two copper toroids; one on either side of the crystal. From an input port, an excitation signal is supplied to the bottom terminal of the $LiNbO_3$

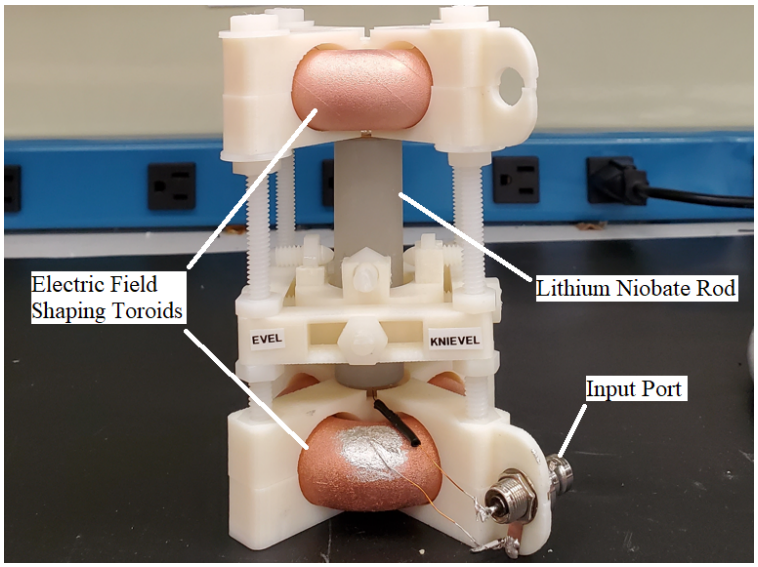


Figure 2.1: Transmitter constructed with lithium niobate rod and copper toroids.

rod. This signal causes mechanical displacements and stress within the crystalline structure. These displacements generate charge via the piezoelectric effect that are then accelerated onto the surface of the top toroid, which is a floating electrode. These accelerated surface charges on the top toroid radiate a dipole-like quasistatic electric field pattern by capacitively coupling to the bottom toroid, which is grounded. An image of this transmitter is shown in Fig. 2.1.

The magnitude of the radiated electric field of one of these devices can be increased by either increasing the Q-factor or by increasing the magnitude of the input excitation signal. $LiNbO_3$ devices are typically limited by the material Q-factor [17], so increasing the excitation signal level is often a desirable option to increase the generated fields. The goal of this research is to study how the radiated electric field magnitude changes with respect to an increasing excitation signal magnitude. Section II provides an analysis of the longitudinal mode resonance as well as an analysis of the transmitter as a whole. Section III describes a high voltage sweep experiment that is performed to study the radiating capabilities of this device and understand where it reaches a state of nonlinearity. Section IV analyzes the results of the experiment, and Section V concludes by noting important observations.

2.2 Length Extensional Resonance and Transmitter Analysis

The piezoelectric element in the transmitter can be represented by Mason's equivalent circuit for a Length Extensional (LE) resonator. The resultant impedance for the LE resonator with free surfaces from Mason's model can be simplified [18–20] with a substitution $f_p = \mathbf{v}_{33}^D/2l$ to find the equation of the free LE resonator,

$$\mathbf{Z}(\omega) = \frac{l}{i\omega\varepsilon_{33}^T(1-\mathbf{k}_{33}^2)A}\left[1 - \mathbf{k}_{33}^2\frac{\tan(\omega/4f_p)}{\omega/4f_p}\right] \tag{2.1}$$

where ε_{33}^T is the free complex permittivity, $\mathbf{k}_{33}$ is the complex longitudinal electromechanical coupling, l is the length of the resonator, A is the resonator cross-sectional area, and f_p is the antiresonant frequency. The equation for the impedance can be simplified further by noting that around the fundamental resonance, the impedance can be matched accurately using a complex circuit model [1] composed of a complex static capacitance $\mathbf{C}_0$, and complex motional inductance $\mathbf{L}_1$ and capacitance $\mathbf{C}_1$, as is shown in Fig. 2.2. C_{T1} and C_{T2} represent the self-capacitance of the top and bottom toroids, respectively, and C_{stray} represents the stray capacitance of the system. The model was found to give a better fit than the typical Butterworth Van Dyke model [1, 21], and matches the resonance equation about both the resonant and antiresonant frequencies. The complex circuit model components were found from the complex effective material coefficients determined from Smits' technique as well as the process outlined in [1], and are provided in Table 2.1.

It should be noted that circuit model shown in Fig. 2.2 can be simplified further by placing the stray and toroid capacitances in parallel with the static capacitance of the piezoelectric

Table 2.1: Complex circuit model parameters

Component	**Real**	**Imaginary**
C_0 (pF)	9.496	-0.032
C_1 (pF)	0.177	-0.00039
L_1 (H)	63.795	0.129

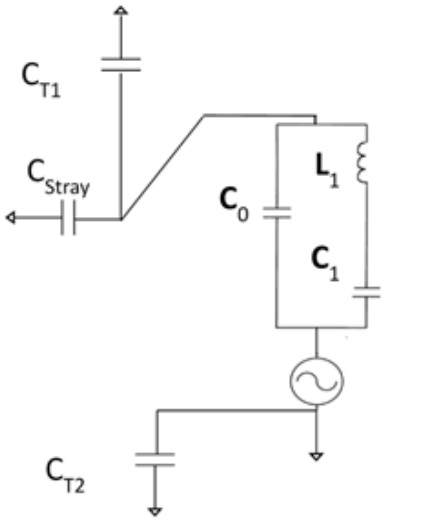


Figure 2.2: Schematic of $LiNbO_3$ transmitter with complex circuit model representing the piezoelectric material.

complex circuit model. This allows adding the stray and toroid capacitances to the static capacitance of the piezoelectric resonance circuit, and suggests that in terms of impedance, the stray and toroid capacitance only affect the baseline impedance of the resonator, which essentially changes only the effective dielectric constant. An initial example of this system incorporated an $LiNbO_3$ rod with gold-plated electrodes and a material density $\rho = 4659$ kg/m^3. The impedance spectrum was measured across the resonator with toroid and stray capacitance, and the data is shown in Fig. 2.3.

The spectrum was analyzed using Smits' method [4] to determine the complex effective material constants of the LE mode. Details on the method for the analysis of the LE mode can be found in [22]. Smits' method utilizes three points on the curve and one typically selects points on the maximum and minimum of the impedance or admittance curves, as well as a clean point on the curve away from any sideband resonances. The results are shown in Table 2.2. These coefficients are effective in that the true free permittivity is increased due to the stray and toroid capacitance, as well as the resonator aspect ratio $r = L/D = 2$, which is smaller than the recommended aspect ratio for material characterization [23]. The nominal data listed is based on [17].

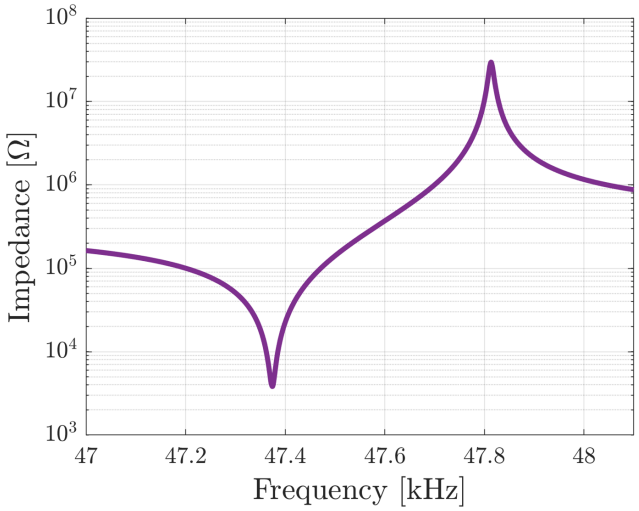


Figure 2.3: Impedance spectrum of $LiNbO_3$ transmitter.

It should be noted that the imaginary component of the piezoelectric coefficient was within the limits discussed by Holland [24]. The effective Q about the resonance was found to be $Q_r = Re[\mathbf{s}_{33}^E]/Im[\mathbf{s}_{33}^E] = 2700$, while $Q_a = Re[\mathbf{s}_{33}^D]/Im[\mathbf{s}_{33}^D] = 450$ for antiresonance. This reduction in Q around the antiresonance has been noted before [1] and is directly related to the imaginary component of the complex coupling constant ($\mathbf{k}_{33}$) through the relationship $\mathbf{s}_{33}^D = \mathbf{s}_{33}^E(1 - \mathbf{k}_{33}^2)$. It should also be noted that the impedance of the resonator exceeded 20 $M\Omega$ at the antiresonant frequency, which increased the noise in the spectra around f_p.

Table 2.2: Material constants determined from Smits' method for $LiNbO_3$ resonator in parallel with stray capacitance and toroid capacitance

Constant	**Nominal**	**Real**	**Imaginary**
$\mathbf{k}_{33}$ (#)	0.168	0.150	8.45×10^{-5}
$\mathbf{s}_{33}^D$ ($\mathrm{pF\,m^{-1}}$)	4.89	4.748	-0.00103
$\mathbf{s}_{33}^E$ ($\mathrm{pF\,m^{-1}}$)	5.026	4.857	-0.00093
$\mathbf{d}_{33}$ ($\mathrm{pC\,N^{-1}}$)	6	15.3	-0.0185
ε_{33}^T ($\mathrm{pF\,m^{-1}}$)	254.1	2155	-7.216

2.3 High Voltage Experiment

To test the hypothesis that increasing the magnitude of the excitation signal increases the magnitude of the radiated quasistatic electric field, we establish our experimental architecture as shown in Fig. 2.4. This experiment was performed outdoors in an area free from intrusive objects and scatterers, providing a clear line-of-sight experimental environment. The separation between transmitter and receiver was kept at a constant distance of 12 m to obtain measurements within the radiating near field of the $LiNbO_3$ transmitter, which is the operating region of interest for this device [14].

As can be seen from the diagram, a sinusoidal input signal is supplied by a Rigol DG4062 Arbitrary Waveform Generator (AWG). The fundamental frequency of this signal is 47.37 kHz, which corresponds to the resonant frequency of the $LiNbO_3$ transmitter, as shown in Fig. 2.3. This signal is then fed into an E&I 1140LA Power Amplifier (PA) which amplifies the magnitude of our input signal by a factor of 900, given the system's impedance. This signal is applied to the bottom terminal of the $LiNbO_3$ crystal, which causes the transmitter to radiate as mentioned previously. The front-end of the receiving subsystem measures the generated electric field signal with a Schwarzbeck Mess-Elektronik EFS 9218 biconical EQS field probe. This probe detects the incoming signal as a voltage level, which is sampled and digitized using a National Instruments USB-6356 Analog-to-Digital Converter (ADC). This data is then sent to a laptop which saves the data and performs Digital Signal Processing (DSP) algorithms to process the data.

The magnitude of the input signal is controlled at the AWG and an initial value of

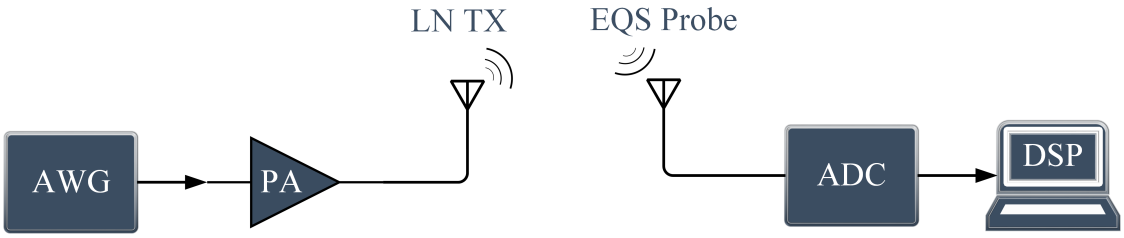


Figure 2.4: Block diagram of high voltage experimental setup.

20 mVpp is selected, which corresponds to an 18 Vpp signal output from the PA to the $LiNbO_3$ transmitter. The electric field data is then captured by the EQS probe, and data is saved. This process is then repeated by increasing the AWG voltage in 20 mV increments until a voltage of 1 kVpp is supplied at the input of the transmitter.

2.4 Results

Upon completion of the excitation signal amplitude sweep, the received electric field versus input voltage plot of Fig. 2.5 is obtained. It is important to note that the input voltage displayed is the amplitude that is supplied from the PA to the bottom electrode of the $LiNbO_3$ crystal, rather than the amplitude that is generated by the AWG. From a qualitative perspective, it can be seen that the electric field behavior is quite linear up to a supplied signal of 100 Vpp. Beyond this point, the slope of the curve decreases, but there is a linear trend until approximately 750 Vpp. Beyond this point, the $LiNbO_3$ transmitter field generation saturates and approaches a state of nonlinearity. Data obtained beyond the limits of this plot varied wildly and were not reproducible, which is highly indicative of nonlinear performance.

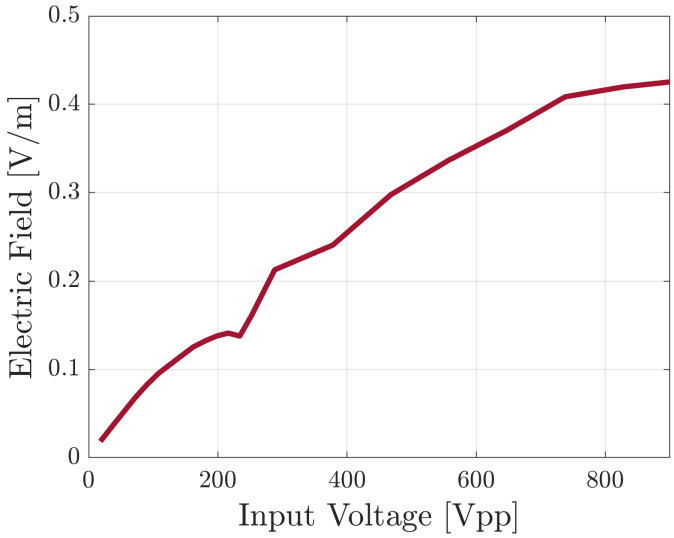


Figure 2.5: Received electric field magnitude as a function of input voltage.

Once it was determined that the $LiNbO_3$ transmitter was operating well into the nonlinear region, the voltage continued to increase to determine how much supplied voltage the device could tolerate before internal stresses became too great, causing the crystal to break. It was witnessed that a supplied voltage of 1.35 kVpp pushed the crystal to its breaking point and caused it to fracture in the center, just below its mounting point. The radiated electric fields generated from these higher voltages were not any higher than those shown in Fig. 2.5.

2.5 Conclusion

This research provides a great deal of insight into the peak-to-peak input voltage that materials of this nature can withstand. Due to the material Q-factor having a limitation on the magnitude of generated electric fields, it is necessary to know the magnitude of the field that can be generated without pushing these devices into a nonlinear operating region. This is especially valuable for low frequency applications in which devices utilizing lithium niobate are sought after for their small form-factor, such as for positioning, sensing, and tracking.

From the result obtained, we conclude that an excitation signal magnitude of less than 100 Vpp is ideal to ensure the $LiNbO_3$ transmitter is operating predictably in its linear region. Although driving these devices at higher excitation magnitudes results in higher radiated fields, operating these devices at high voltage for extended periods of time can often depole the crystal and subject it to other unwanted hysteresis effects [11]. The results obtained help to better understand the radiation performance of $LiNbO_3$ transmitters as well as their limitations. Additionally, these results provide insight that may be helpful to others wishing to utilize this technology for different applications.

CHAPTER 3

Electric Field Pattern Measurements of 82 kHz Lithium Niobate Transmitters

3.1 Introduction

Frequencies ranging from 30 kHz to 300 kHz are classified as LF. Despite limited bandwidth, LF offers reliability, deep signal penetration in objects, and resistance to jamming, making it ideal for various applications including underwater and underground communications, as well as quasistatic indoor position sensing. Despite these benefits, the use of small and portable LF antennas results in low efficiency due to inherent constraints on radiation efficiency and quality factor for such antennas [13]. Recent advancements in mechanical antenna development has facilitated the exploration of new applications in the VLF and Low LF range that were previously not feasible with traditional wire dipole antennas [12,14–16,25,26]. The key distinction between conventional electrically small antennas and mechtennas lies in their operational mechanisms. Conventional antennas generate dynamic electromagnetic fields through the acceleration of charges, whereas mechtennas produce time-varying radiated fields by physically moving, rotating, or oscillating electric charges or magnetic dipole moments [15].

The key factor for achieving high efficiency in mechanical antennas is the advancement of a mechanical oscillatory system with a high-quality (high-Q) factor, characterized by minimal damping and effective coupling to changing dipole moments. Many of the proposed mechtennas employ either rotating electric or magnetic dipoles, or utilize piezoelectric materials driven at acoustic resonance to generate radiation at low frequencies. Many studies have demonstrated that acoustically driven piezoelectric crystals operating at resonance can

be used to generate quasistatic electric fields in the LF band with efficiencies that are orders of magnitude greater than conventional electrically small antennas [14, 16, 26].

In this work we make use of a Y 36° cut lithium niobate rod with longitudinal mode resonance around 82 kHz as an electroquasistatic transmitter for indoor positioning and navigation applications. It is necessary to characterize the near field patterns of such transmitters to understand the effect of the surrounding environment on their behavior as well as the coupling between different transmitters in a multi-axial system. Since conventional methods cannot be used to measure near field patterns in the LF regime, a simple parallel plate-based setup was developed. The standard method for testing devices via well defined fields is using the TEM cell technique [27]. In the low frequency limit (approximately <30 MHz) and for large devices, the parallel plate technique may be preferred, which was widely employed in the 1960s [28]. Such a technique can be considered as the electric field analog of the well-known Helmholtz coil. In section II, the fundamental principle of operation of the experimental setup is explained, and results from electromagnetic simulation conducted to verify measurement setup are also presented. Section III follows by presenting the measured electric field patterns of the piezoelectric transmitter at 82 kHz. To the best of the authors' knowledge, it is the first time such near field pattern measurements have been performed on low frequency piezoelectric transmitters.

3.2 Principle of Operation and Simulations

The near field pattern measurement setup consists of two metallic capacitor plates attached to two platforms separated by a fixed distance. At the center of the plates is a rotating platform to mount the Device Under Test (DUT). The plates are excited with a signal generator at the frequency of interest and the voltage received at the DUT for each angle of rotation is sampled using an NI DAQ. The whole system is controlled using a laptop and the resultant field patterns are plotted. Fig. 3.1 shows the schematic of the setup.

The DUT is constructed with a lithium niobate (LN) crystal and two aluminum toroids. The crystal is 4 cm long and has a diameter of 2 cm, which results in a longitudinal mode

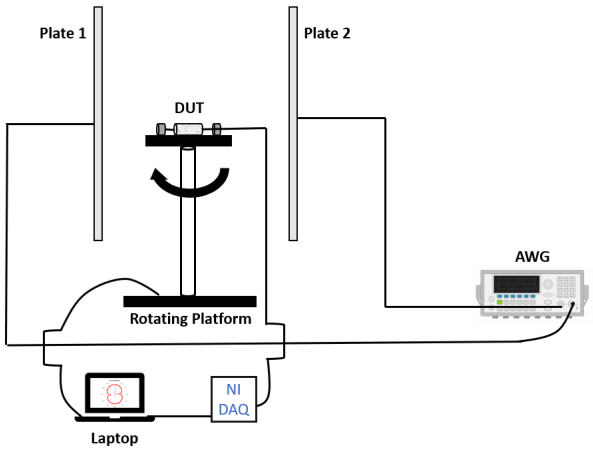


Figure 3.1: Schematic of the measurement setup.

resonance at 82 kHz. The bottom toroid is grounded and the top toroid is floating, but capacitively coupled to the bottom ground toroid. This toroidal configuration ensures a dipole-like radiation pattern in both the transmit and receive modes. It is to be noted that in the measurement setup the DUT acts as a receiver. As the DUT is rotated in the experimental setup, the applied electric field between the plates induces a mechanical oscillation of charges within the piezoelectric crystal at the resonant frequency which leads to an accumulation of charges on the surface of the toroids. These mechanical displacements cause stress within the crystal that are then converted to electrical energy via the piezoelectric effect. This electrical energy can be detected as a voltage at the port of the DUT. An image of the DUT is presented in Fig. 3.2, and a further explanation of the functionality of this type of device can be found in [14].

3.2.1 Electric Field Distribution, Simulation, and Analysis

As stated previously, the principle of using parallel plates to generate uniform electric fields is analogous to that of using Helmholtz coils to generate uniform magnetic fields. For the case of the Helmholtz coil [29, 30], current is supplied to two identical coils placed at a carefully selected distance from one another to ensure that a uniform magnetic field is generated at the center. Similarly, if we supply voltage to two identical metal plates placed close to one

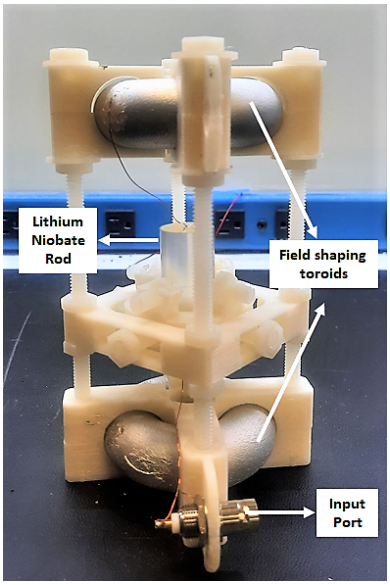


Figure 3.2: Acoustically driven mechtenna constructed with lithium niobate rod and aluminum field-shaping toroids.

another relative to the dimension of the plates, a uniform electric field can be generated between the plates [31]. The potentials on the plates can be either V^+/V^- or V^+/GND. One of the constraints in the setup is determining the distance between the plates. If they are too close then the DUT will experience large ground planes which result in the measurement setup affecting the DUT performance. If the plates are too far from one another, then fringing fields distort the uniformity of the field between the plates.

To analyze this trade-off, we establish a simulation in FEKO and solved for the field distribution between the two plates. The simulation setup and result are shown in Fig. 3.3. For this particular simulation, frequency was set to 82 kHz, W/d was set to 1 by using 1m square plates separated by 1m. An excitation voltage of 1V was applied between the two PEC plates using a wire port. The result shown in Fig. 3.3 is as expected since the charges rush to the edges of the plates, creating a more concentrated electric field. Also, if we ignore the edge effects temporally and assume electrostatic condition, the electric field between the plates is simply

$$E \approx \frac{\Delta V}{\Delta y} \tag{3.1}$$

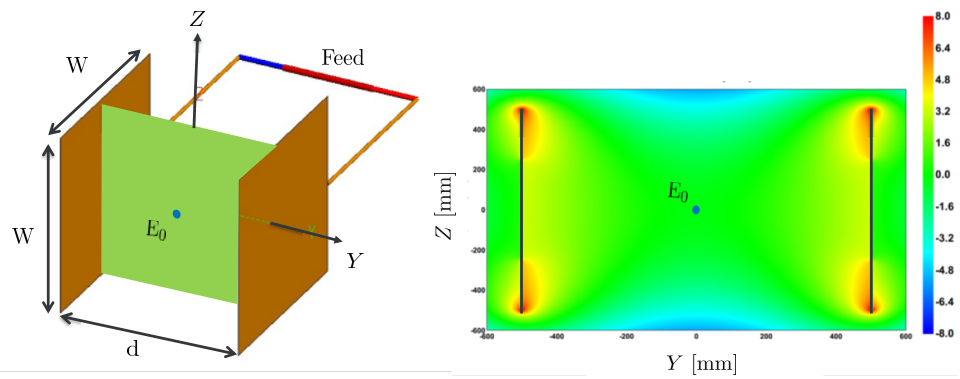


Figure 3.3: FEKO simulation setup (left) and results (right).

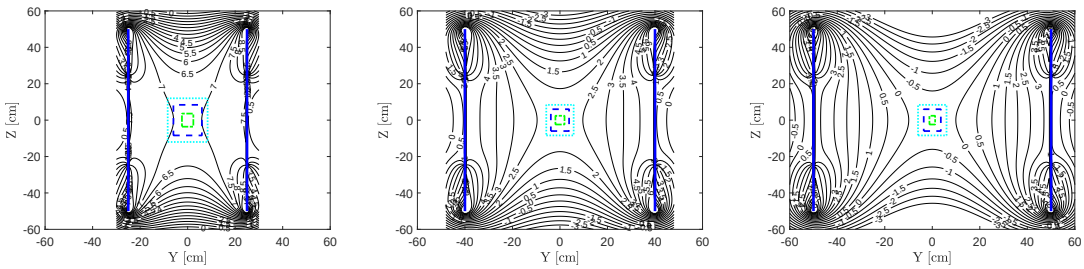
where V is potential and y is distance between the two plates. For the simulation, $\Delta V = 1V$ and $\Delta y = 1m$. Thus, $E = 1V/m = 0$ dBV, which aligns with the simulation results.

Although the qualitative level of field homogeneity shown in the simulation could be sufficient for some applications, we were interested in obtaining quantitative values. We then exported the FEKO results and used MATLAB to analyze the field distribution. In Helmholtz coil literature, homogeneity is typically expressed in (%) [32], while parts-per-million (ppm) is more commonly used in MRI to quantify magnetic field distributions [33]. Adopting both cases, the expression for electric field homogeneity is as follows

$$\text{Homogeneity [\%]} = \frac{\Delta E}{E_0} \cdot 10^2 = 10^4 \text{ Homogeneity [ppm]} \tag{3.2}$$

where E_0 is the reference electric field. In our case it is the field at the center point between the two plates, as shown in Fig. 3.3. ΔE is the difference between electric field at any point and the reference ($|E - E_0|$). So the question is, what is the area or volume of a region where the field distribution is most likely to have homogeneity with a constant value, or less than a certain value, relative to our reference point. We consider area since the problem is symmetric due to square plates. This region of interest (ROI) ultimately determines how large the DUT can be if a certain level of field homogeneity is required.

Fig. 3.4 show the results for the proposed question and Table 3.1 outlines the numerical values. For a simple analysis, we choose three different ppm values (1k, 5k, 10k) as well as



(a) (b) (c)

Figure 3.4: Electric field distributions between parallel plates. Boxes show 1k, 5k, 10k ppm areas. (a) $d/W = 0.5$, (b) $d/W = 0.8$ and (c) $d/W = 1$

three values for d/W (0.5, 0.8, 1). In Fig. 3.4 the square boxes show the corresponding ppm regions. From these results a couple of observations can be made. Namely, that the area of each box is inversely proportional to level of homogeneity inside the box, as expected. Also, as d/W increases, the area of the fixed homogeneity level decreases as a result of fringing fields becoming a major factor due to increased plate separation. These two observations help to formulate a trade-space for the level of homogeneity that can be achieved with a reasonable size and separation of the plates. The simulation was repeated for a few more d/W values and a trade-space was created, as shown in Fig. 3.5

It is clear that d/W needs to be as small as possible to guarantee the required level of field homogeneity in ROI depending on the application. As noted earlier, however, if the plates are too close then the DUT will experience ground effects. The piezoelectric transmitter, as an example, is designed and fabricated to resonate at 82 kHz,

Table 3.1: Selected values of ROI Area for different d/W values and homogeneity levels

Homogeneity (ppm)	ROI Area (cm^2)		
	$d/W = 0.5$	$d/W = 0.8$	$d/W = 1$
1000 = 0.1%	42	21	22
5000 = 0.5%	221	115	106
10000 = 1%	430	236	211

which is in the quasistatic regime in this scale. If the highly conductive plates get too close to the transmitter, they could easily detune the resonant frequency. Being a high-Q device, the voltage at the terminals will drastically decrease when detuned. Because of this, caution is needed when choosing d/W values for the plates to ensure that there is no interference with the performance of the DUT.

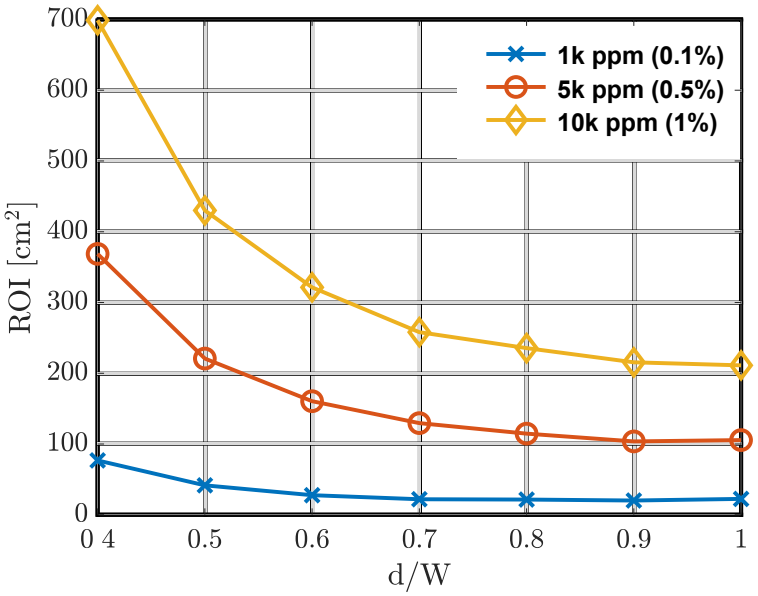


Figure 3.5: Trade-space showing size/separation of plates vs ROI for 3 homogeneity levels

3.3 Near Field Pattern Measurements

To demonstrate the efficacy of this experimental setup in obtaining near field pattern measurements of our LN transmitter, we supply a 10V peak differential sinusoidal input signal to each plate with an arbitrary waveform generator. We set the plates 1m apart to obtain a known electric field magnitude of 20 V/m at the center of the plates via (3.1). The fundamental frequency of the input signal is chosen to be identical to the resonant frequency of our DUT, which was measured with an impedance analyzer to be 82.08 kHz. It is essential that the generated field operates precisely at this frequency because the DUT has a high mechanical Q-factor, and thus a very narrow bandwidth of resonance. The DUT is placed on a custom-built platform that rotates 360° via a stepper motor, as shown in Fig. 3.6. It

is important to note that the DUT is placed horizontally to ensure that the dipole moment of the LN crystal is aligned along the axis of the electric field generated by the plates at the 0° position. This stepper motor is controlled by a MATLAB script that slowly increments the angle of rotation until a complete rotational cycle is complete. The port on the DUT is then connected to an NI DAQ module that samples, processes, and displays the received data with the same script controlling the motor.

After a complete revolution of the DUT in the experimental setup, we obtain the received power pattern shown in Fig. 3.7. This near field radiation pattern has maxima normal to the applied electric field, with minima orthogonal to the field. The obtained results resemble a typical pattern of dipole moment.

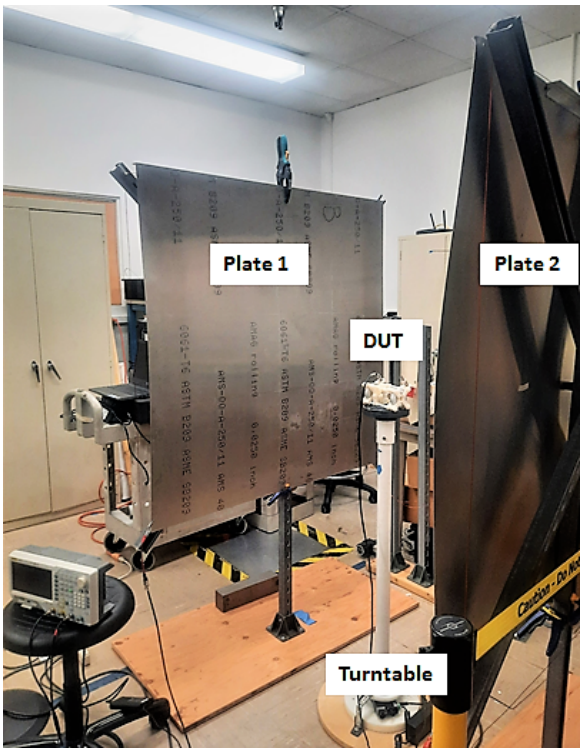


Figure 3.6: Experimental setup showing DUT mounted on turntable along the direction of the Electric field.

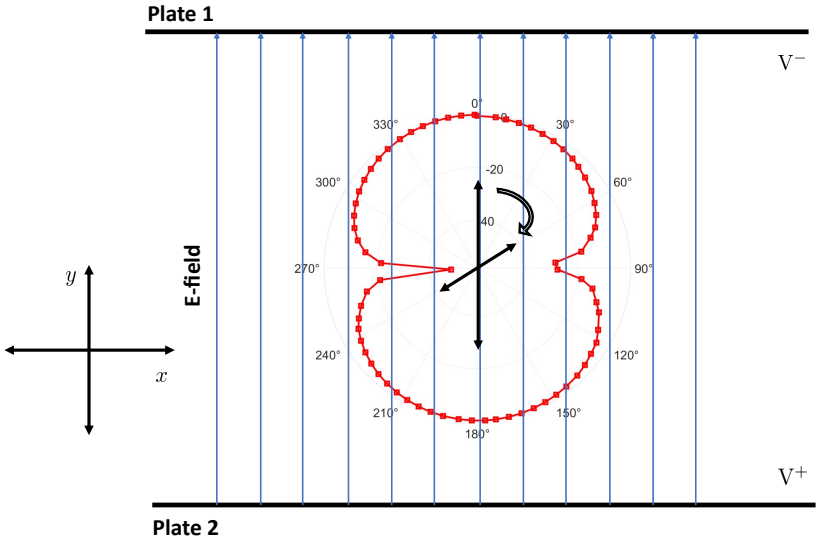


Figure 3.7: Normalized power pattern for DUT operating at resonance. Arrows at the center indicate rotating dipole moment of DUT. Parallel lines show alternating electric field between the plates captured at $t = 0$

3.4 Conclusion

A simple and easy-to-use setup was presented to measure the near field electric field patterns of acoustically driven piezoelectric transmitters in the LF regime. Dipole-like field patterns of Y 36° cut lithium niobate transmitter were successfully measured at 82 kHz. We conducted trade-space analysis of the measurement setup and provided simulation results on the relations between plate size/separation and field homogeneity. It is to be noted that this setup is not limited to measuring patterns from piezoelectric emitters, but has broad applications including EMI/EMC characterization and pattern measurements of electrically small antennas in the VLF and LF range.

CHAPTER 4

Pushing Acoustically-Driven Transmitters to the MHz Regime

4.1 Introduction

Radars are crucial remote sensing tools in both Earth and planetary sciences, as well as in various societal applications such as military, commercial, energy, and industry sectors for sensing. Sounding radars, a principal type of active radar, utilize lower frequencies—usually below 100 MHz—to explore the ionosphere, Earth's subsurface, and the interiors of other planetary bodies. Among the various examples, MARSIS (Mars Advanced Radar for Subsurface and Ionospheric Sounding) is notable for its low-frequency operations, as low as 1.3 MHz, allowing it to penetrate up to 3 km into Martian polar ice, significantly advancing our understanding of water and ice on Mars. This capability requires a 40 m long antenna and about 400 W of power delivered to the antenna for radio transmission [34]. The requirement for such a large antenna and high power is due to fundamental limits in antenna efficiency that restrict the minimum size of an antenna and the maximum power that can be radiated due to matching limitations [13, 35].

However, recent advancements in acoustically-driven piezoelectric structures offer promising improvements. These new devices achieve significant efficiency gains and can operate at much smaller sizes than traditional systems. Specifically, transmit antennas with $L \ll \lambda$ have been developed to bypass the earlier challenges posed by bulky, inefficient matching networks and the low radiation resistances typical of electrically small antennas (ESAs). These advancements enable efficiencies up to 10^5 times higher at frequencies above 1 kHz, bypassing the need for traditional matching elements and overcoming the Bode-Fano bandwidth

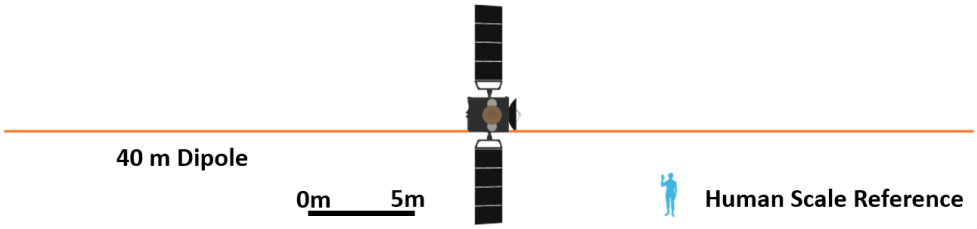


Figure 4.1: Size of the MARSIS sounding radar antenna (horizontal line) compared to the spacecraft and a human silhouette.

limit [14]. This breakthrough could enable more compact and efficient radar systems for both planetary and terrestrial applications, potentially revolutionizing the field by reducing the physical footprint and power requirements of future radars [36].

Additionally, recent research by Beauchamp et al. [37] explores the potential of airborne ground penetrating radars (GPRs) to detect groundwater in hyper-arid regions. They conclude that airborne GPRs can effectively explore groundwater when using low radar frequencies (10 MHz or less), coupled with effective ground clutter rejection and a medium or higher vadose zone soil resistivity. Implementing piezoelectric transmitters in such applications could further enhance these systems, allowing for the miniaturization of antenna systems while maintaining or even increasing efficiency and depth of penetration.

In this work, we examine the performance of lithium niobate ($LiNbO_3$) transmitters exhibiting quasi-thickness extensional mode resonance at 1 MHz. To the best of the authors' knowledge, it is the first time that acoustically-driven transmitters have been demonstrated and analyzed in the MHz regime. Two different configurations of crystals are studied: one with ring electrodes and another with fully-plated electrodes. In Section II, we discuss the theory behind piezoelectric transmitters and present the complex circuit model. Section III presents and analyzes the impedance profile of our transmitters. Section IV describes the outdoor line-of-sight radiated near field drop-off experiment and the results obtained therefrom. Section V estimates the radiation efficiency of these devices and compares to those of similarly sized conventional electrically small dipole antennas. Conclusions based on the measured results are presented in Section VI along with a discussion of how this

technology can be advanced for future integration into compact radar systems.

4.2 Method of Operation

The transmitter prototype consists of a $LiNbO_3$ crystal placed in between two metal toroids, as shown in Fig. 4.2. Continuous wave excitation is supplied with one terminal connected to the bottom electrode of the $LiNbO_3$ crystal. The other terminal of the supply is connected to the bottom torus, which is a 3D printed aluminum structure that is grounded. The top electrode of the crystal is then connected to the top aluminum torus, which is left floating. An image of the prototype is presented in Fig. 4.3.

As the input source supplies an electrically oscillating sinusoid, mechanical deformations occur within the crystal in the form of stress and strain [38]. The induced stress and strain cause the $LiNbO_3$ to act as a piezoelectric charge generator. As the crystal generates a large amount of charge, the charge then accelerates on the surface of the top torus, resulting in electromagnetic radiation, the power of which is determined by the Larmor formula:

$$P = \frac{q^2 a^2}{6\pi\varepsilon_0 c^3} \tag{4.1}$$

where q is the charge, ε_0 is the permittivity of free space, a is the acceleration of the charged particle, and c is the speed of light. Due to the reverse polarity of the bottom torus, the electric field is shaped from torus-to-torus, resulting in an electric field pattern similar to that of a conventional dipole antenna [14, 16, 38, 39].

The key advantage in using these devices is that since the velocity of acoustic waves is five orders of magnitude lower than the speed of light, it results in resonant operation at frequencies five orders of magnitude lower than similarly sized conventional antennas. Such acoustically-driven antennas can offer orders of magnitude higher efficiency compared to similarly sized electrically small conventional dipoles [14]. This improvement in efficiency can be maintained well into the MHz range by piezoelectric arraying [38], which can significantly improve the radiated electric field for more power intensive applications, such as

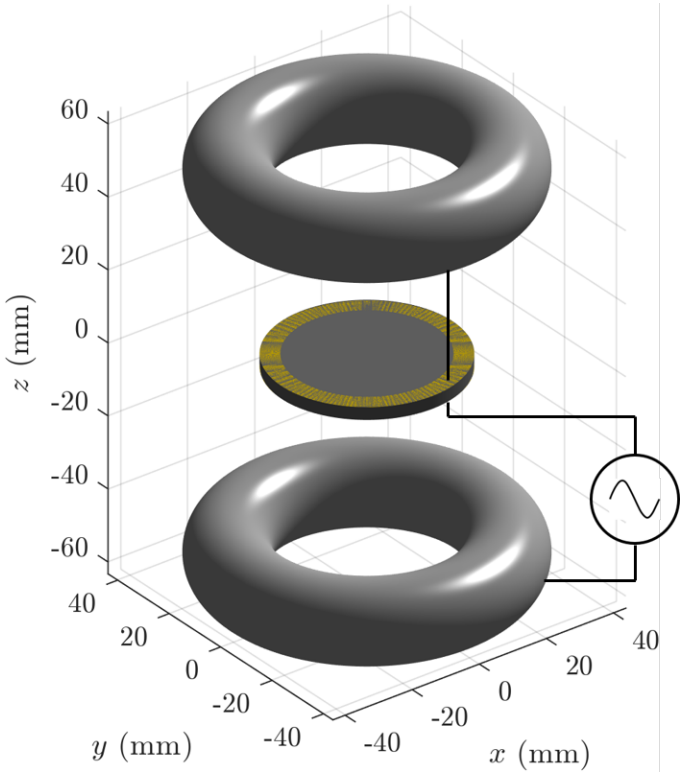


Figure 4.2: Wiring configuration diagram of $LiNbO_3$ transmitter.

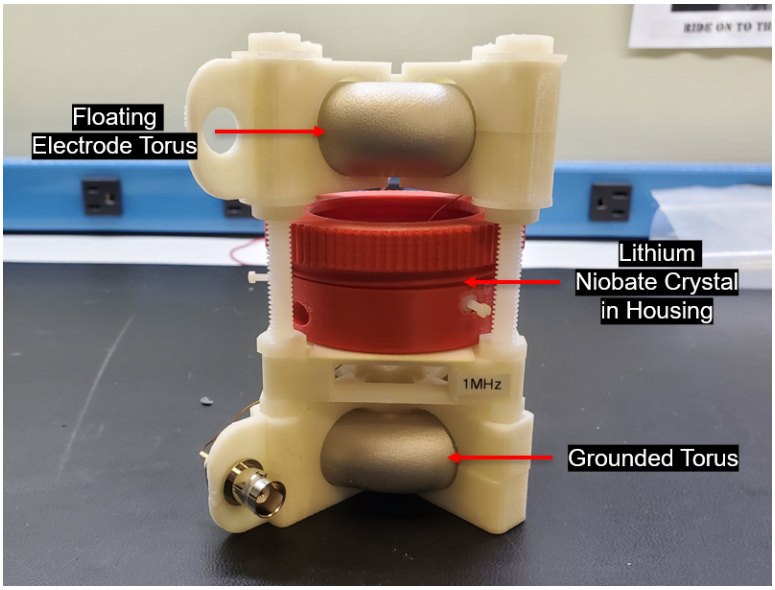


Figure 4.3: Lithium niobate piezoelectric transmitter with 3D-printed toroidal radiating mechanisms.

radar systems. It is noted, however, that acoustically driven transmitters are narrow band systems because of their high quality factors (Q-factors), and direct antenna modulation techniques [14, 38] will need to be implemented for them to be used as radar transmitters.

Piezoelectric transducers can have multiple different modes of vibration including radial, length-extensional, thickness extensional, and shearing modes [11]. The maximum achievable radiated power from a piezoelectric antenna is limited by the maximum charge density achievable on the surface of the transducer before the breakdown of the surrounding medium. This can be achieved by using piezoelectric material of high dielectric constant, by enclosing the antenna in a medium with higher breakdown voltage than air, or by using field-shaping toroids or spheres near the surface of the piezoelectric antenna. The thickness-extensional mode of vibration can be exploited in $LiNbO_3$ crystals to generate electromagnetic radiation in which the resonant frequency is determined by the dimensions of the crystal. The dielectric constants of $LiNbO_3$ are $\varepsilon_{11} = \varepsilon_{22} = 44 \times 10^{-12}\,\mathrm{F/m}$ and $\varepsilon_{33} = 29 \times 10^{-12}\,\mathrm{F/m}$, which are comparatively lower than other materials like lead zirconate titanate ($\varepsilon_s > 1000 \times 10^{-12}\,\mathrm{F/m}$), and hence the design in [14, 26, 40] makes use of electric field-shaping toroids to prevent breakdown of the surrounding air and maximize the radiated field strength. This single-ended feeding technique, with the use of field-shaping toroids, decreases the peak surface electric field for a given dipole moment, thereby increasing the achievable peak electric field before breakdown.

We make use of the same technique with a sample of $LiNbO_3$ that is fabricated to have a 10° rotated Y-cut orientation with thickness of 3.5 mm and a diameter of 50.9 mm. Although the dimensions of this crystal are not ideal for pure thickness extensional mode resonance [41], it ensures a small form-factor while still exhibiting a quasi-thickness extensional mode resonance at 1 MHz. This comes as an extension of previous work operating in the kHz regime [3, 39] with length-extensional resonators.

Previous research has indicated that the electrical charge generated by mechanical stress within the piezoelectric crystal is neutralized by the electrodes on the surface of the crystal, so it is ideal to design electrodes that are around the edge of the surface where stress is the lowest [16]. This is to allow the section of crystal with the highest stress and highest

charge density to radiate more freely. Because of this, we study transmitters constructed with both fully-plated and ring-plated electrodes, as shown on the left and right of Fig. 4.4, respectively. Comparing the radiation characteristics of both will help to verify this assertion.

Efforts have been made to develop circuit models for these devices based on their radiated electric field [26], but we choose to use the complex circuit model developed for piezoelectric resonators [1, 22]. Such circuit models provide intuitive understanding of the system and prove as effective tools in verifying certain properties of the system. This circuit model is shown in Fig. 4.5 and is represented by a capacitor in parallel with a capacitor and an inductor that are in series. It is important to note that the capacitance and inductance values are all complex, which reliably predict the resonant behavior of piezoelectric transducers around the fundamental thickness extensional mode.



Figure 4.4: Lithium niobate crystals resonant at 1 MHz in fully-plated electrode configuration (left) and ring electrode configuration (right).

4.3 Resonant Transducer Analysis

Before analyzing the radiation characteristics of these acoustically-driven transmitters, small signal impedance measurements were performed to understand the resonance behavior of each transmitter. Due to the high-Q nature of these devices, it is expected that each transmitter prototype will have a slightly different resonant frequency. Because of this, it is

necessary to analyze the resonant behavior of each device separately.

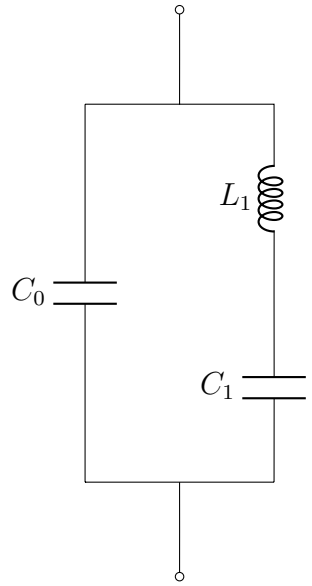


Figure 4.5: Complex circuit model for piezoelectric resonators [1].

To do so, we connect each transmitter to an impedance analyzer with a probe calibrated up to the input port. The resonance frequency f_s is determined as the frequency in which the impedance is entirely real. The obtained impedance spectra of the fully-plated crystal transmitter and the ring-electrode crystal transmitter are shown in Figs. 4.6a and 4.6b, respectively. As we can see, the fully-plated crystal transmitter is more resistive near its resonance than the ring-electrode transmitter. This additional resistance is partly due to the extra gold plating on the electrodes that is not present on the ring-electrode lithium niobate sample. Additionally, we note that the spectrum is much cleaner on the ring-electrode impedance spectrum. The side band resonances in these spectra are potentially due to mounting reaction forces and coupling to radial and ring modes in the piezoelectric element. It should also be noted that the geometrical aspect ratio may not be sufficient for isolation of the thickness mode from the lateral modes for such a high-Q sample.

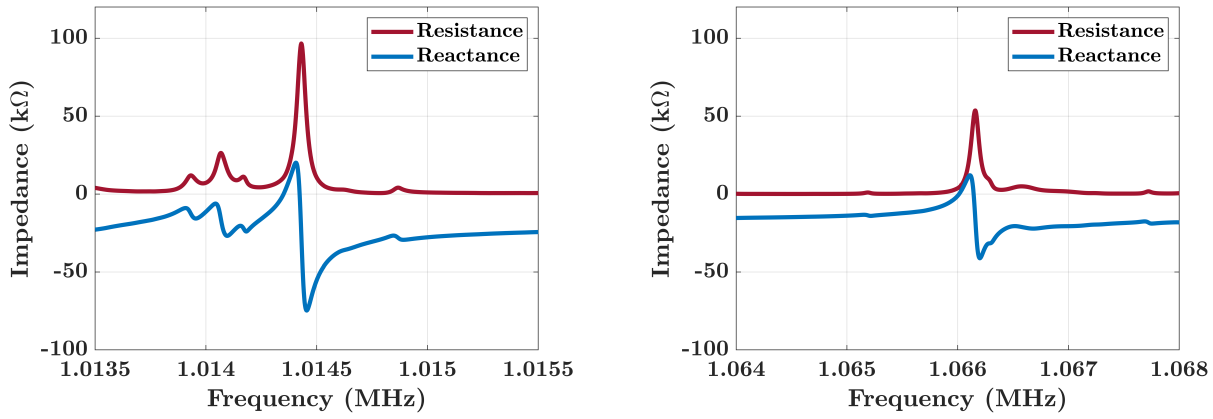
The Q-factor of each device is estimated by fitting the spectra using Smits' method for the thickness extensional resonance [3, 4] and taking the ratio of the real component of the effective elastic constant to the imaginary component. The effective complex material coefficients were then used along with the $LiNbO_3$ geometry to determine the complex circuit

components using the transforms developed by Sherrit et. al. [1], and the resultant components are shown in Table 4.1. We observe that the complex capacitance for each transmitter is on the order of 10 pF, whereas the complex inductance is relatively large, on the order of 20 H. Additionally, we note that the ring-electrode transmitter is more capacitive and less inductive than the fully-plated transmitter. It should be noted that the circuit parameters in Table 4.1 describe the electrical behavior of the full piezoelectric antenna including the $LiNbO_3$ sample, mounting structure, toroids, and connectors.

Table 4.1: Complex circuit model component values derived from material coefficients using Smits' method [3, 4], and from geometry and equations provided by Sherrit et al. [1].

Component	**Fully-Plated TX Value**	**Ring-Electrode TX Value**
C_0	$(5.9373 - j0.52764)$ pF	$(9.2115 - j0.17796)$ pF
C_1	$(1.00621 - j0.1992)$ fF	$(2.6966 + j0.07155)$ fF
L_1	$(23.545 + j4.6594)$ H	$(8.26044 - j0.2198)$ H

The Q value about the resonance frequency f_s was determined using the effective short circuit elastic stiffness parameter c_{33}^E of the full system by fitting the data to the thickness extensional mode resonance. The small signal resonance frequency f_s of the ring electrode transmitter was 1.0662 MHz while the f_s of the fully-plated transmitter was 1.0144 MHz. The slightly higher resonant frequency is likely due to the higher stiffness in the thickness mode of a disk compared to a ring. The effective electromechanical coupling was $k_t = 0.018$ for the ring element antenna and $k_t = 0.015$ for the full disk element antenna. The Q-factor of our system was estimated by dividing the real part of elastic stiffness parameter $Re\left(c_{33}^E\right)$ by the imaginary component $Im\left(c_{33}^E\right)$. We did this for both the fully-plated and ring-electrode crystal transmitters, and obtained Q-factors of 14.1×10^3 and 13.9×10^3, respectively. We note that the high-Q nature of these devices produced a very narrowband resonance, which is apparent from the impedance spectra of Fig. 4.6.



(a) (b)

Figure 4.6: Impedance spectra at resonance of lithium niobate transmitter (a) with fully-plated crystal and (b) with ring electrode crystal.

4.4 Near Field Transmission Measurements

With knowledge of the resonant behavior of these devices at low input signal levels, we aim to drive these devices at higher input voltage levels to obtain direct line-of-sight near field drop-off measurements. Our goal is to observe the drop-off behavior of the transmitted field as a function of distance. Specifically, we aim to compare the performance of the fully-plated crystal transmitter to the ring-electrode crystal transmitter with the intention of determining which configuration yields higher transmitted field.

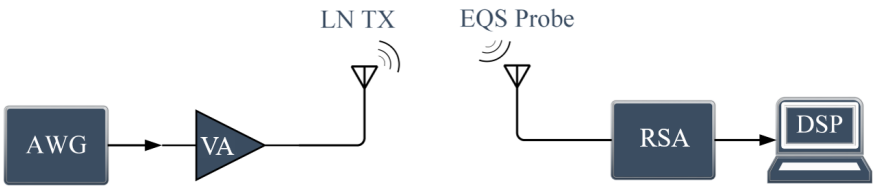


Figure 4.7: Block diagram of the electric field drop-off experimental setup.

The experiment began with positioning our $LiNbO_3$ transmitters in an unobstructed outdoor setting. A biconical EQS field probe was aligned one meter away from the transmitter, matching the dipole moment of the transmitter. This probe was connected to a real-time spectrum analyzer (RSA) to display the received power as a function of frequency. The

setup included a signal generator connected to the transmitter to perform a frequency sweep around the resonant frequencies identified earlier with an impedance analyzer. The input voltage was set to 20 Vpp to facilitate the observation of the resonant behavior under increased voltage levels. By applying a max-hold function on the RSA during the frequency sweep, the resonance peak of each device was clearly observed and used to determine the driving frequency for the experiment.

Following this determination in driving frequency, we established the experimental configuration as depicted in Fig. 4.7. A continuous wave (CW) signal was generated using an arbitrary waveform generator (AWG) set to the specific resonant frequencies—1.0149 MHz for the fully-plated transmitter and 1.066 MHz for the ring-electrode transmitter. The signal was then amplified to 100 Vpp via a voltage amplifier (VA). This amplified signal drove the transmitter, facilitating EQS radiation which was captured by the EQS probe and analyzed by the RSA. An image of our experimental setup is shown in Fig. 4.8.

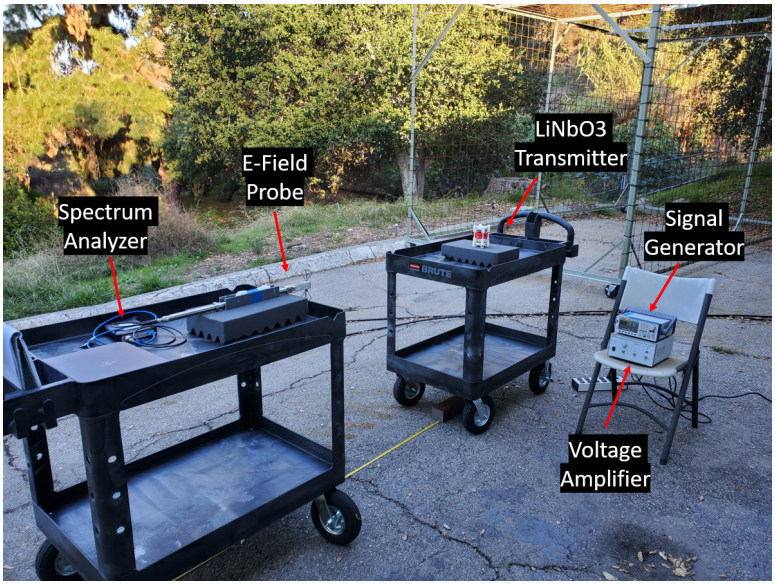


Figure 4.8: Experimental setup for electric field drop-off measurements, depicting the positioning of the transmitter and EQS probe.

This setup was used to perform measurements at varying distances from 1 meter up to 15 meters from the transmitter, and the data is shown in Fig. 4.9. The data indicates that the ring electrode configuration radiated approximately 10 dB more field across all distances

compared to the fully-plated configuration. This finding demonstrates the effectiveness of optimizing electrode placement to sections of the crystal under lower stress, enhancing radiation efficiency while preventing charge neutralization by the electrodes. Additionally, we compare both sets of measured data with a simple theoretical model in which the $LiNbO_3$ transmitter field decays as $1/r^3$. The measured field response agrees quite well with the predicted near field drop-off model expected for an electric dipole.

These results indicate that transmitters with ring electrode configurations are more effective for applications requiring higher field transmission, suggesting the potential benefits of deploying such devices in an array configuration for enhanced performance.

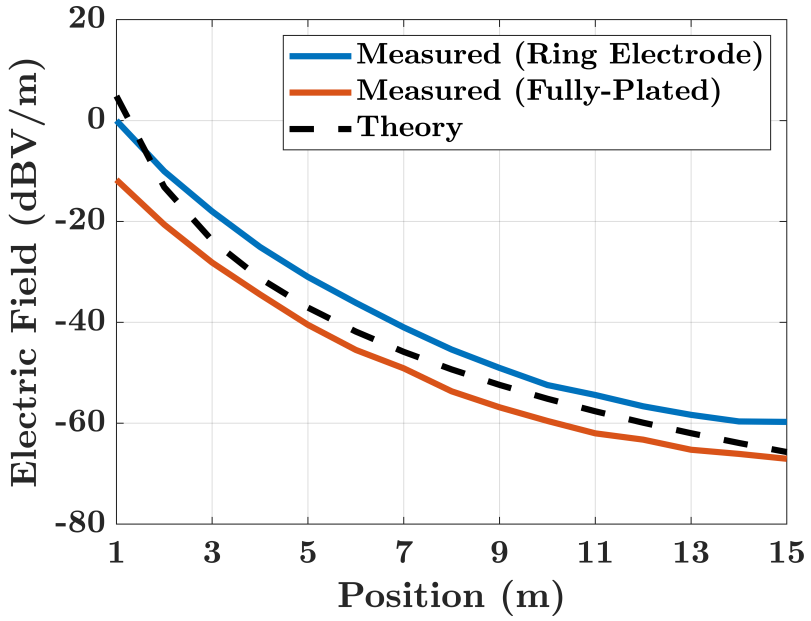


Figure 4.9: Comparison of electric field from fully-plated transmitter and ring electrode transmitter in an outdoor line-of-sight environment.

4.5 Radiation Efficiency Estimation

Now that we have observed the resonant behavior of these devices as well as the field drop-off trend in a direct line-of-sight environment, we wish to estimate the efficiency of these devices and compare to that of a similarly sized electrically small dipole antenna (ESA) operating

at 1 MHz. We do this based on the well known Chu's limit for the theoretically minimum radiation quality factor Q_a of an antenna with wave number k contained within a sphere of radius a [14, 42], as given by (4.2).

$$Q_a = \frac{1}{ka} + \frac{1}{(ka)^3} \tag{4.2}$$

First, we estimate the efficiency of the piezoelectric transmitter as $\eta = Q_m/Q_a$ where Q_m is the measured Q-factor of the device with the ring-electrode crystal. The obtained efficiency at 1.066 MHz is 4.31×10^{-5} as tabulated in Table 4.2. We repeat the same calculation for a passive antenna assuming Q_m of 200 which is practical for dipoles at 1 MHz. It is to be noted that the dimension a is assumed as 65.25 mm, which is half the overall length of the piezoelectric transmitter from torus to torus for both the cases. We obtain an efficiency of 6.20×10^{-7} for the ESA, as tabulated in Table 4.2.

As we can see, the $LiNbO_3$ transmitters are estimated to have efficiencies two orders of magnitude greater than that of a similarly sized dipole ESA. With these results, it is quite apparent that these piezoelectric transmitters are much more efficient radiators than dipoles of the same size even at MHz frequencies. This is especially important at an operating frequency in the low-MHz regime, where antennas are typically quite large and inefficient. These piezoelectric transmitters can allow for more efficient radiation in a much smaller form-factor. Additionally, it is anticipated that arraying these devices and implementing direct antenna modulation schemes will result in stronger radiated field and increased radiation efficiency.

Table 4.2: Calculated radiation efficiency values at 1 MHz.

Device	**Radiation Efficiency at 1 MHz**
Electrically Small Dipole	6.20×10^{-7}
$LiNbO_3$ Transmitter	4.31×10^{-5}

4.6 Conclusion

Through this study, we have found that piezoelectric transmitters operating at 1 MHz can radiate quasistatic electromagnetic waves effectively in a close-range line-of-sight environment. Additionally, we have shown that transmitters utilizing samples of $LiNbO_3$ with ring-shaped electrodes on the top and bottom result in greater radiated fields than those utilizing fully-plated electrodes. The reason for this lies in the fact that confining the electrodes to the outer edges of the crystal ensures that the area of highest charge density is exposed, allowing much more charge to accelerate on the surfaces of the toroids. Covering this region with electrodes results in neutralized charge, and thus less radiated field.

Additionally, we compared the efficiency of these devices to that of a similarly sized electrically small dipole antenna, and found that radiation efficiency is greater by two orders of magnitude at this operating frequency. From these findings, it is clear that these piezoelectric transmitters show a great deal of promise in providing high radiation efficiency in a small form-factor in the MHz range of frequencies.

The results of this study serve as a starting point for the development of small form-factor radiators in the low-MHz regime. To enhance the radiated field and efficiency of these devices, further research is needed to study the effects of arraying these devices and implementing direct antenna modulation techniques for use as radar transmitters. Achieving these results would make this technology a viable option for integration into radar and remote sensing applications that require low frequency operation while maintaining high radiation efficiency.

CHAPTER 5

Transition to Quasistatic Magnetic Field Positioning

5.1 Introduction

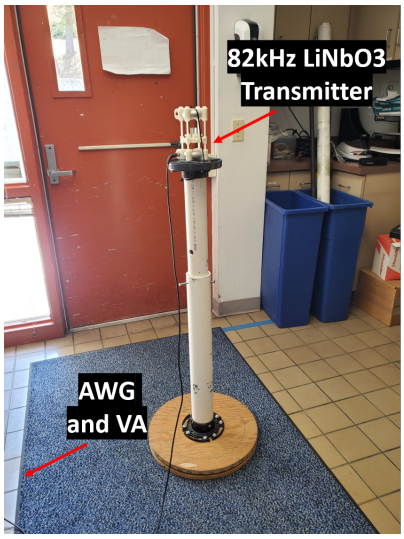
The research up to this point has been largely based on studying the radiation characteristics of piezoelectric transmitters generating quasistatic electric fields. Understanding the field patterns and operating voltage range, we now aim to observe the field decay and attenuation in steel-reinforced structures. For these devices to transmit fields for a position-sensing system, it is necessary for their generated fields to propagate deep within these structures. This chapter includes measured results from an indoor drop-off experiment for a $LiNbO_3$ transmitter radiating EQS fields at a resonance of 82 kHz. It is shown that the fields radiated from these devices attenuate too quickly in steel structures. This indicates that an alternate method of field generation is necessary for adequate signal coverage and reliable position-sensing.

In response to this adjustment, it is determined that magnetic systems, which have been shown to work in previous systems [43–50], are more reliable, prompting a shift in system architecture. Since magnetic systems aren't limited in tunability like high-Q piezoelectric transmitters that have very narrow resonances, broadband frequency sweeps are performed indoors to observe the frequency dependence of field propagation. These results determine that 3 MHz is a frequency supported for strong field strength penetrating through thick metal walls. This serves as a preliminary step in system architecture design and hardware development for our multiaxial position-sensing system.

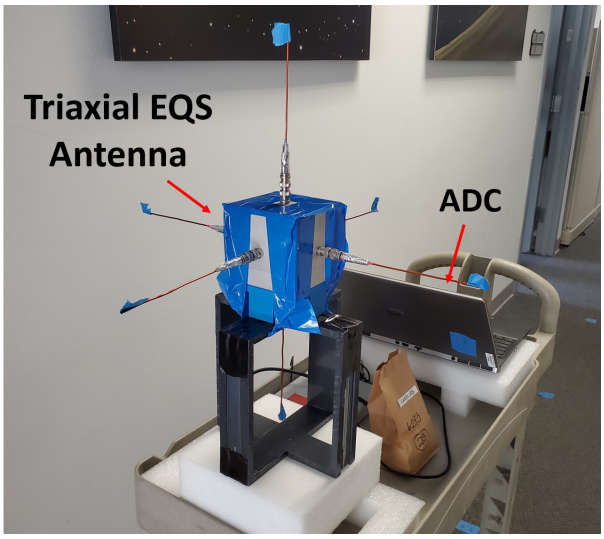
5.2 Piezoelectric Transmitter Range Limitations

In the pursuit of utilizing $LiNbO_3$ transmitters for M/EQS position-sensing, we choose to operate at a resonant frequency of 82 kHz. The reason for this is because this resonant frequency results in a geometric aspect ratio of 7 cm length to 2 cm diameter, which ensures quasi-length extensional mode resonance and results in a predictable dipole-like field pattern [39]. This is also a desirable resonant frequency because it is close to the operating frequency of the first version of POINTER.

We wish to observe the field decay within a steel-reinforced structure. This will give us some insight into signal attenuation caused by the building. To observe this behavior, we set up our $LiNbO_3$ transmitter inside a steel-reinforced building, as shown in Fig. 5.1a. An AWG generates a CW signal with frequency corresponding to the resonant frequency of the piezoelectric transmitter. This signal is then amplified with a VA to a peak-to-peak signal level of 100 V, which has been shown to make these devices operate in a fairly linear regime [3]. The radiated EQS fields are then received by our EQS receiver, shown in Fig. 5.1b.



(a) 82 kHz $LiNbO_3$ transmitter on platform for indoor field decay experiment.



(b) Multiaxial EQS receiver obtaining indoor field decay measurements.

Figure 5.1: Experimental setup for 82 kHz $LiNbO_3$ transmitter field decay measurements.

This receiver features a multiaxial antenna composed of three orthogonal dipoles. A voltage is then induced at each of these three ports, which is digitized with an ADC and processed with MATLAB. The received electric field magnitude is then obtained based on

$$E = \frac{V}{AF} \tag{5.1}$$

where V is the induced voltage at each port of the multiaxial receive antenna, and AF is the antenna factor corresponding to that axis. These antenna factor values were obtained experimentally using a well-calibrated electric field probe and the electric field pattern measurement system described in [39].

With the $LiNbO_3$ transmitter placed inside the building, the receiver is then moved away from the transmitter in a straight line with data being collected at 1 meter increments. With this data collected, we then model our EQS field decay as

$$E(x) = \frac{\beta \cdot e^{-\alpha x}}{x^3} \tag{5.2}$$

where x is the distance between transmitter and receiver, α is the attenuation constant particular to the steel-reinforced structure environment, and β is a linear scaling factor. This model describes the typical $1/r^3$ piezoelectric transmitter near field drop-off along with an added exponential decay term accounting for building attenuation. A MATLAB script is then developed that determines the values of α and β that results in minimal error between measured data and this theoretical model.

Plotting the measured EQS field drop-off data with the best theoretical model results in Fig. 5.2. It is noted that this is a truncation of data extending to a distance of 20 meters where received field magnitude in negligible. The α and β values that correspond to this theoretical decay model are tabulated in Table 5.1. From this, we obtain an attenuation constant of 1.66, which results in a steep drop-off of EQS fields within this structure. In fact, it is seen that the electric field strength drops to zero at a distance of only 7 meters. This results in subpar coverage that is not ideal for a position-sensing system. To provide accurate and reliable positioning, it is necessary to generate stronger fields that are sustained by the

physical structure of the building. Due to the limitation of transmitter input voltage to ensure linear generation of EQS fields [3], we cannot supply arbitrarily high voltage without pushing the piezoelectric crystal into a highly nonlinear regime. From this, it is clear that we need to transition to an alternate position-sensing system architecture.

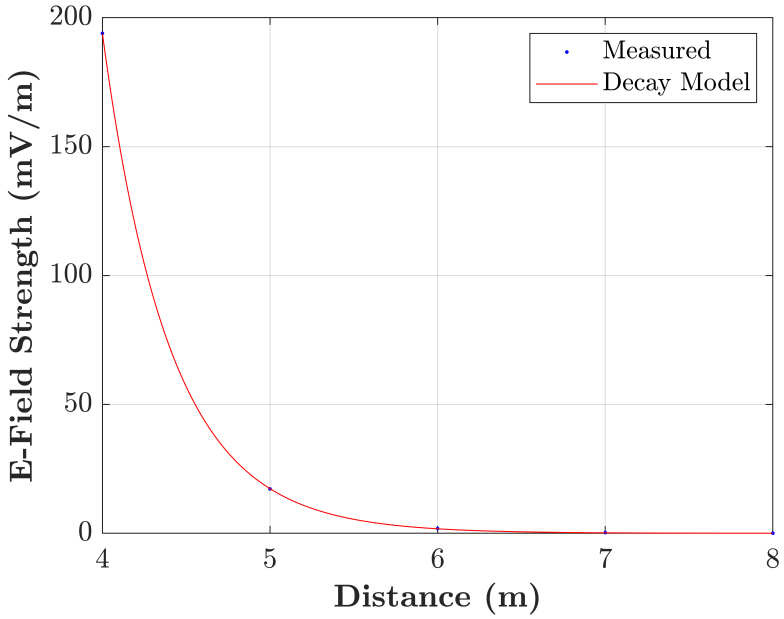


Figure 5.2: Near field drop-off of 82 kHz $LiNbO_3$ transmitter compared to exponential decay model.

Table 5.1: Best fit parameters describing 82 kHz $LiNbO_3$ transmitter field decay in steel-reinforced structure.

Model Parameter	**Parameter Value**
α	1.66
β	9492.5

5.3 Broadband Magnetic Field Sweeps and Frequency Selection

Due to the range limitations of $LiNbO_3$ transmitters, we make the decision to transition from a M/EQS system to a system utilizing MQS fields exclusively, since they have been

shown to work in several configurations [43–50]. It is suggested that increasing the radiation frequency may result in signals that are better supported by the structure of the building. This supposition is analogous to frequencies residing above a certain cutoff frequency for a particular mode to be supported in a rectangular waveguide.

To generate MQS fields, we establish an architecture as shown in Fig. 5.3 in which an RF signal generator (RFSG) is sent to a PA biased with 24V from a DC power supply, then delivered to an off-the-shelf broadband loop antenna. This loop radiates magnetic fields induced by current flowing through the loop. These generated fields are then captured by a broadband loop antenna at the receiver. This signal is then amplified by an internal low noise amplifier (LNA) and received by a portable spectrum analyzer that captures the received spectrum, which is then processed with simple DSP algorithms. We establish a frequency sweep on the RFSG that sweeps from 1 MHz to 30 MHz in kHz-level steps. The intention is to observe the frequency response at several discrete points within the steel-reinforced building to determine if there is an optimal frequency that results in best coverage and SNR.

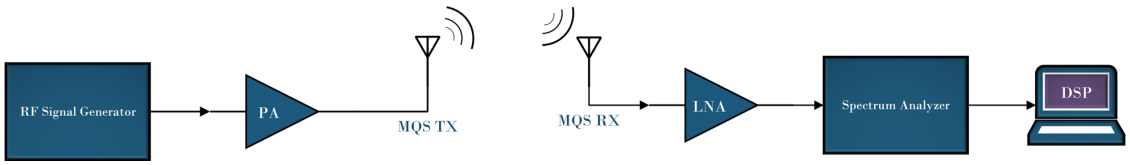
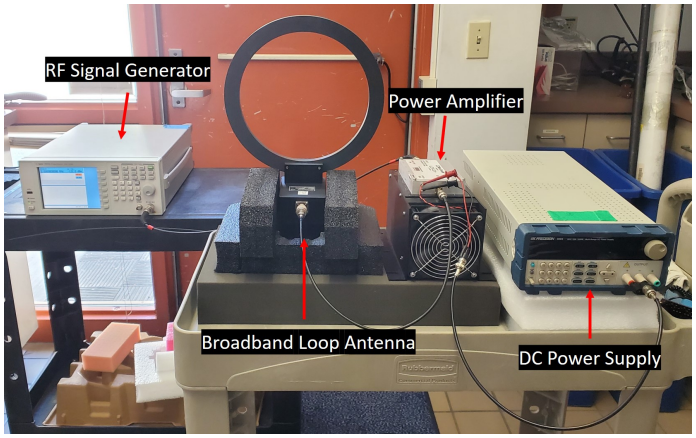


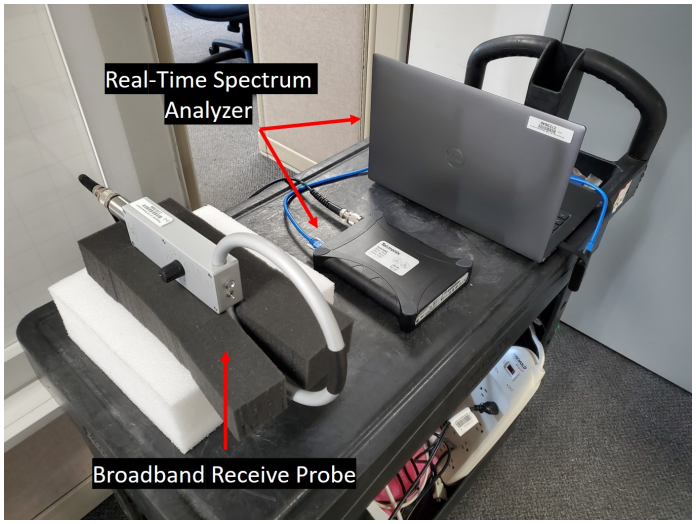
Figure 5.3: Block diagram of single-axis MQS system.

We construct our transmitter and receiver setups as shown in Figs. 5.4a and 5.4b, respectively. We note that the magnetic moments of the transmit and receive loop antennas are aligned for this experiment, which results in greatest power obtained at the receiver. From here, we began our experiment and obtained spectra of frequency sweeps at distances of 5, 9, 13, and 17 meters away from the transmitter. This experiment results in the spectra shown in Fig. 5.5. From this, it is clear that frequencies about 8 MHz are highly unsupported in this structure. Beyond this point, the received power density hits the noise floor of the receiver, which is indicated by the levelling off of power density.

What is most important about this data, however, is that there appears to be a peak in received power at a frequency of 3 MHz for all of the distances in which measurements were



(a) Transmitter setup



(b) Receiver setup

Figure 5.4: Setup of transmitter and receiver for broadband measurements.

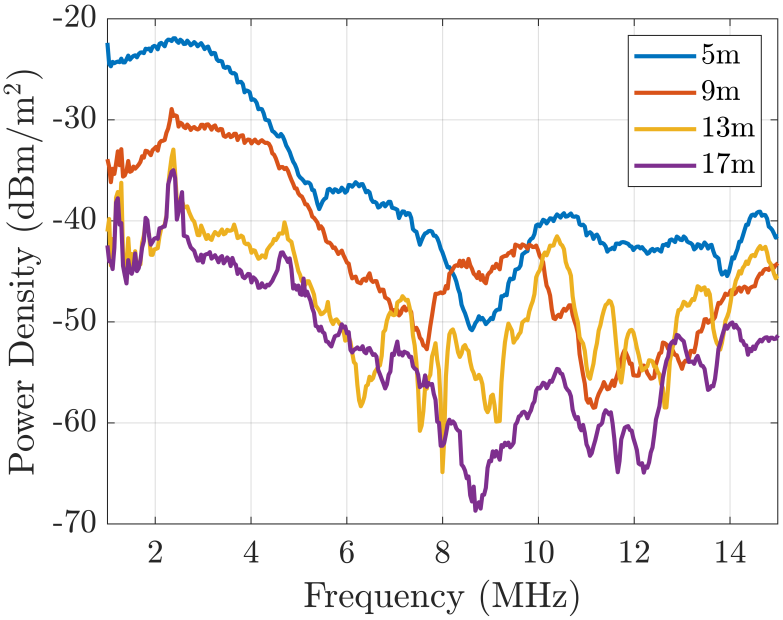


Figure 5.5: Received power density drop-off as a function of frequency at four discrete distances from transmitter.

obtained. After this, there is a steep attenuation in received power density as a function of frequency. These results indicate that an operating frequency of 3 MHz is an ideal candidate for our MQS position-sensing system.

5.4 Conclusion

In this section, we observed the EQS radiation of a $LiNbO_3$ transmitter operating at 82 kHz within a heavily steel-reinforced building. We found that the received electric field strength drops off too quickly with respect to distance due to the attenuative nature of the building on these waves. From here, we determined to transition from a M/EQS system to a MQS to improve the ability to develop a position-sensing system with adequate signal coverage in buildings of this type. We then established a single-axis MQS system architecture with off-the-shelf components and lab equipment. From here, we performed broadband frequency sweeps in the MHz regime to determine that an operating frequency of 3 MHz provides the best signal coverage within this steel-reinforced building. The next step in this process is

extending to a multiaxial system integrated with positioning algorithms.

CHAPTER 6

Quasistatic Magnetic Field Positioning in Single-Story Steel-Reinforced Building

6.1 Introduction

With the discovery that $LiNbO_3$ transmitters radiating at 82 kHz do not provide enough signal coverage in steel-reinforced buildings, we reach the need for a re-design in system architecture. From our previous findings in Chapter 5, we know that MQS radiation around 3 MHz seems to be a good operating region to ensure increased signal recovery and signal-to-noise ratio (SNR). This work presents the design of a multiaxial MQS transmitter and receiver system for position-sensing. The architecture is then realized in the form of several mobile transmitter units and a backpack receiver unit. The MQS system is also integrated with a stereoscopic camera having on-board barometer and inertial measurement unit. It is demonstrated that the system can accurately predict the position of an individual navigating through a heavily steel-reinforced building. The success of this system in accurately predicting positioning resulted in a live demonstration in which positioning is predicted in real time.

6.2 Multiaxial System Architecture and Hardware Development

The limitations of our EQS transmitters necessitated a shift in direction and a readjustment of our system architecture. Instead of using collocated $LiNbO_3$ transmitters and loop antennas as initially planned, we transition to a system utilizing multiaxial loop antennas exclusively. In the previous Chapter, we developed a simple single-axis architecture with lab

equipment to perform broadband sweeps, determining an optimal operating frequency of 3 MHz in these structures. From here, we scale our design to three orthogonal axes at the transmitters and three orthogonal axes at the receiver.

We develop our transmit chain as shown in Fig. 6.1. The chain outputs three separate signals from different ports of a RFSG. We choose these to be CW signals of differing center frequency, which will help with future algorithm development to extract position from received magnetic field power. Each of these signals is then sent to a separate power amplifier and subsequently radiated from one of the axes of a multiaxial loop antenna.

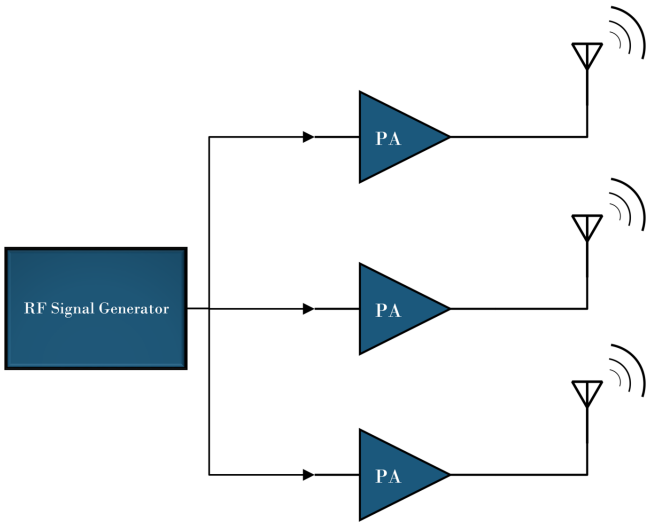
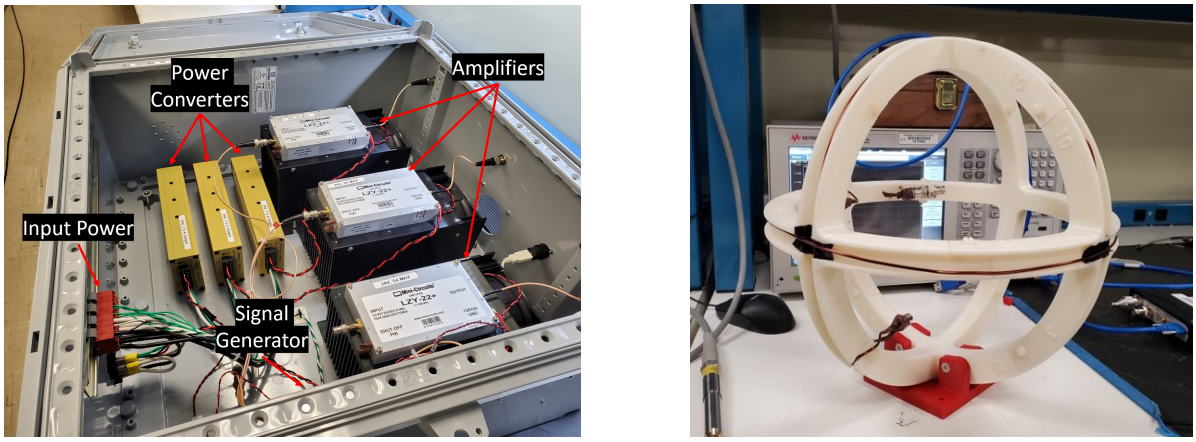


Figure 6.1: Block diagram of multiaxial MQS transmitter.

We realize our transmitter electronics as shown in Fig. 6.2a. Our electronics are installed in a plastic box for portability to ensure easy transportation to different locations for test and measurement. This form-factor also results in consistent wiring, which eliminates the need to connect and disconnect components for each measurement trial. This transmitter contains a single plug to connect to the main AC voltage supply. The incoming AC voltage is then routed to four AC-to-DC converters, three of which convert to an output DC voltage of 24 V and one which converts to an output DC voltage of 3.3 V. The 24 V supplies are used to bias each of the PAs whereas the 3.3 V supply is used to power the RFSG.

Each of the power amplifiers takes an input from one of the ports of the RFSG. We utilize a signal generator that is easily re-programmable, ensuring quick reprogramming in



(a) Transmitter electronics.

(b) Multiaxial loop antenna for transmitter.

Figure 6.2: Development of multiaxial transmitter electronics and antenna.

situations where adjustment to center frequency is necessary, such as environments where the 3 MHz frequency range may have unwanted interference. The output ports of the PAs then lead to BNC ports on the outside of the box that each of the three axes of the transmit antenna connect to.

Our multiaxial transmitter loop antenna is shown in Fig. 6.2b and is supported by a 3D printed structure made of acrylonitrile butadiene styrene (ABS). This antenna is designed to be broadband to ensure signal reception not limited to a single resonant frequency. This is to allow the offset frequencies corresponding to the different antenna axes to radiate with approximately the same strength. To ensure this operation, we design each axis of the loop antenna to have a natural resonance that is sufficiently higher than our center frequency of 3 MHz, ensuring that the resistive loss at the frequency of operation is minimal, resulting in strong current flow through each wire loop of the antenna.

The dimension of each axis is chosen to be approximately 1 foot in diameter to satisfy a trade-off between antenna size and induced magnetic moment magnitude. Each axis consists of a single turn of 12 AWG copper magnet wire, ending in an unbalanced BNC connector. Measuring the resonance of each axis on an impedance analyzer results in the resistance and reactance spectra shown in Fig. 6.3 and tabulated in Table 6.1. From this, we see that each axis has a natural resonance slightly above 50 MHz, with peak resistance of greater than 10

kΩ. This operation results in a very low resistance at a frequency of 3 MHz.

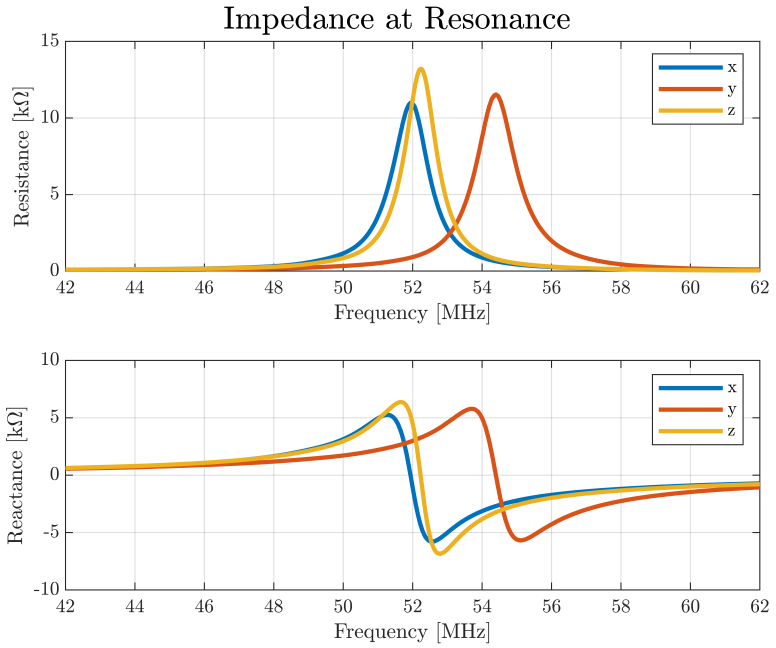


Figure 6.3: Impedance spectra of transmitter loop antenna axes at resonance.

Table 6.1: Natural resonant frequency of each transmitter loop antenna axis.

Axis	**Resonant Frequency (MHz)**	**Resistance at Resonance (kΩ)**
x	51.95	10.99
y	54.4	11.54
z	52.24	13.22

Next, we transition to the design and construction of our MQS receiver. We extend our single-axis receive chain to what is shown in Fig. 6.4. Each axis of the multiaxial loop antenna receives electromagnetic energy that is routed to a LNA, filtered with a band-select filter, and sent to an individual port on a portable oscilloscope. This data is then processed to extract the peak combined power from all transmitted signals, which will be used in position-sensing algorithms to predict instantaneous position.

Just like the transmitter, our receiver electronics are also realized with off-the-shelf components, as shown in Fig. 6.5a. Our multiaxial receiver loop antenna is shown in Fig. 6.5b.

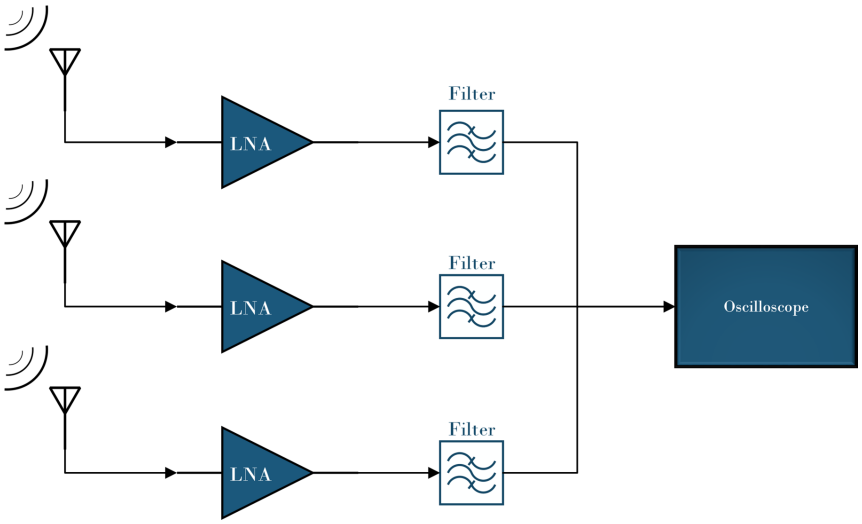
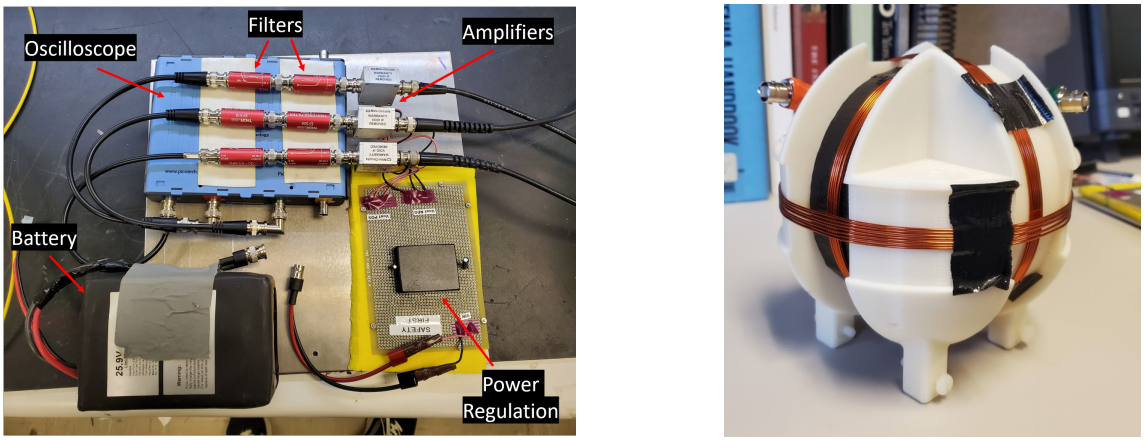


Figure 6.4: Block diagram of multiaxial MQS receiver.

Each axis of the receive antenna receives electromagnetic energy that is sent to one of the LNAs, filtered with a low-pass filter and high-pass filter in series, then sent to a small oscilloscope that is controlled by a laptop (not shown). Half of the electronics are dedicated to power management, and consist of a 25 V DC lithium-ion battery that is regulated to 15 V with an off-the-shelf DC-to-DC converter. This supplies the necessary biasing to each of the LNAs.



(a) Receiver electronics.

(b) Multiaxial loop antenna for receiver.

Figure 6.5: Development of multiaxial receiver electronics and antenna.

Each axis of our receive antenna is constructed with seven turns of 18 AWG copper

magnet wire. Each of these axes varies slightly in diameter due to the design of our 3D printed ABS structure requiring offsets to ensure the wires of each axis do not touch the wires of orthogonal axes. The diameter of each loop axis is tabulated in Table 6.2. This antenna is also designed to operate in a broadband manner, receiving tones of varying frequency without significantly filtering them due to resonant operation. Each axis is connectorized similar to that of the transmit antenna, with unbalanced BNC ports. Baluns were tested at the receive antenna ports during the design process, but it was found that this led to no improvement for this system architecture. The impedance spectra of each axis is measured with an impedance analyzer, and is shown in Fig. 6.6. Additionally, the natural resonant frequency of each loop is tabulated in Table 6.3 along with the resistance at resonance. We conclude that having natural resonances at these frequencies is sufficient for broadband signal reception.

Table 6.2: Loop diameter of each axis of multiaxial receiver antenna.

Axis	**Loop Diameter (cm)**
x	12.9
y	11.6
z	14

Table 6.3: Natural resonant frequency of each receiver loop antenna axis.

Axis	**Resonant Frequency (MHz)**	**Resistance at Resonance (kΩ)**
x	14.19	170.97
y	15.26	199.27
z	13.22	215.42

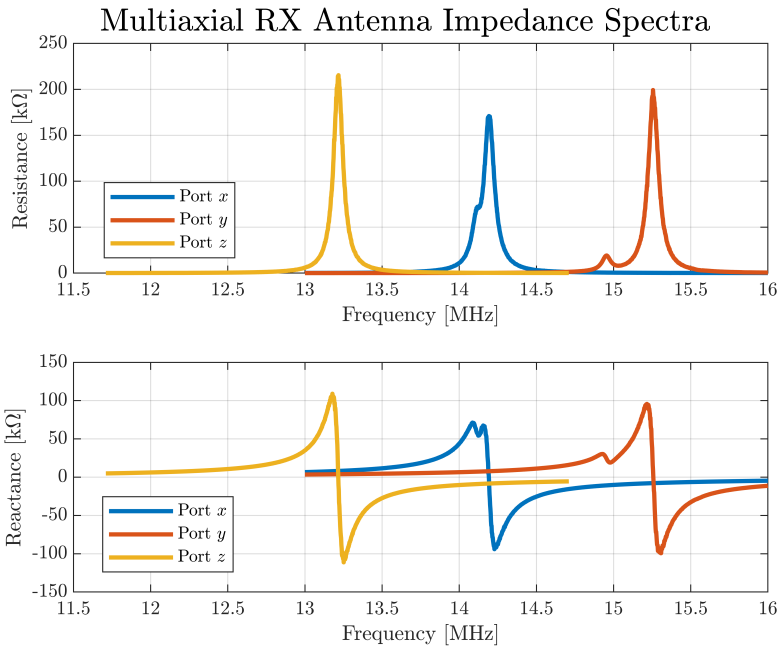
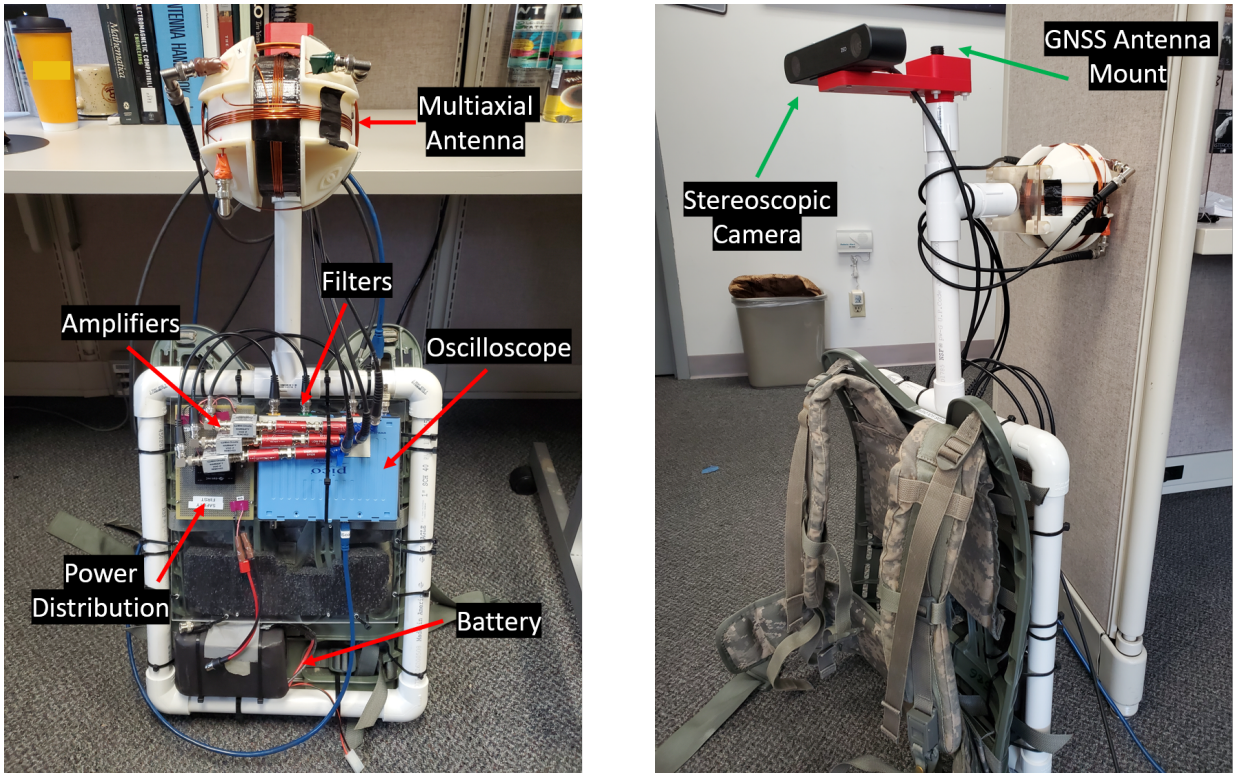


Figure 6.6: Impedance spectra of receiver loop antenna axes at resonance.

6.3 System Integration and Sensor Fusion

Now that we have designed the system architecture and developed the transmitter and receiver hardware, we next move forward to the integration of our system. Specifically, we integrate with computer vision to provide redundancy to positional prediction in environments that are not completely obstructed from field-of-view. We choose to utilize a stereoscopic camera with on-board inertial measurement unit, barometer, and accelerometer. We also developed a custom data collection program that combines received magnetic field data with computer vision camera data. From here, we develop our MQS receiver hardware into a backpack form-factor to be easily transported by the user.

We develop the structure of our portable receiver unit as shown in Figs. 6.7a and 6.7b. We assemble a military-grade backpack frame that contains shoulder straps and a waistband to make the receiver ergonomic. A PVC frame is then assembled and connected to the backpack. The receiver electronics are mounted on a slab of sturdy acrylic that is connected to the backpack and PVC frame. Extending from the top of the PVC frame is a PVC pole that connects to custom 3D printed mounts to hold the receive antenna, the stereoscopic



(a) Rear view of receiver electronics.

(b) Side view of camera module and GNSS antenna mount.

Figure 6.7: Mobile receiver unit used for real-time position sensing.

camera, and a global navigation satellite system (GNSS) antenna to be integrated for future development. This will allow us to map relative coordinates obtained from the MQS system to global reference coordinates.

The integration of the MQS subsystem and the computer vision subsystem is performed in Python and uses APIs available for both the portable oscilloscope and the camera. A graphical user interface (GUI) is developed that combines the received power of each individual tone transmitted and plots versus distance from the transmitters. Additionally, positioning data is obtained from the camera, and previous camera position data is saved for reference.

This system integration was performed in preparation for a single-story positioning demonstration in which position is predicted in real time. For this demonstration, we built two transmitters with identical components and radiation performance. Each transmitter radiates three different tones that are placed 10 kHz apart, with center frequency of all tones residing at 3 MHz. For this demonstration, we develop a simple algorithm that collects positioning data from the camera and receives total magnetic field power corresponding to each of those positions.

Our algorithm first collects data, then performs a coordinate transformation to set the starting point of data collection as an arbitrary (0,0) point for our coordinate system. This is performed with the following coordinate system transformation:

$$\begin{bmatrix} x' \\ y' \end{bmatrix} = \begin{bmatrix} \cos(\theta) & -\sin(\theta) \\ \sin(\theta) & \cos(\theta) \end{bmatrix} \begin{bmatrix} x \\ y \end{bmatrix}$$

where (x,y) are the original coordinate values from the camera and (x',y') are the corrected values for our relative coordinate frame. Next, the predicted magnetic field is determined based on

$$F(x', y') = e^{-\alpha x'} \times e^{-\beta y'}$$

where $F(x', y')$ is the received magnetic field strength at (x',y'). A MATLAB script is

developed that is optimized to find the α and β values corresponding to a minimized error between our theoretical model and our measured magnetic field power. From here, we convert to magnetic field power in dBm by performing the following conversion:

$$P_{\text{dBm}}(x', y') = 10 \cdot \log_{10}(|F(x', y')|^2).$$

To test our system integration, we place two transmitters outside of a steel-reinforced building and transmit six tones that are spaced 10 kHz apart and centered at 3 MHz. We then collect data by walking in a 2D grid through the building. From this, we obtain the data shown in Fig. 6.8. In these plots, the positional data points are determined from the camera, and the color bar corresponds to the magnetic power received by the MQS positioning system. We display our measured data along with the results from our theoretical model and the estimated error in dB between the two sets of data. From these results, we see that there is small error between the theoretical data and the measured data at most distances, except in close range. These results show promise in our approach of modeling field decay in heavily steel-reinforced buildings, but there is additional work to improve the close-range accuracy.

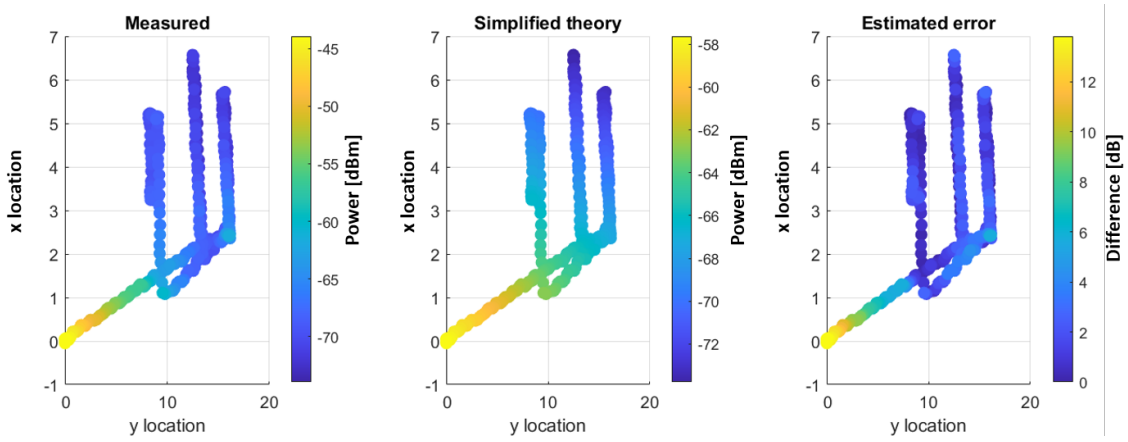


Figure 6.8: Comparison of measured positioning data with theoretical model.

6.4 Live Position-Sensing Demonstration and Results

The previous section demonstrated the results of integrating our MQS position-sensing system with computer vision data acquisition. We developed an exponential decay model that predicts magnetic power drop-off in steel-reinforced structures adequately deep within the building, but not at close range. Because of this, we switch to a fingerprinting approach for our demonstration. This method relies on using previous measurements to determine future positioning [51]. Although this method of positional prediction will not work in any arbitrary building without previous data collection, it serves as a starting point for developing more advanced positioning algorithms. Ultimately, a third transmitter is required to develop a more robust position-sensing system that operates based on the principles of triangulation.

For this system demonstration, we place two transmitters outside a single-story steel-reinforced structure exactly as done previously. An image of one of our positioned mobile transmitter units is shown in Fig. 6.9. We then navigate with our backpack system as shown in Figs. 6.10a and 6.10b. This system was used to collect initial data within the building that serves as the reference look-up table for our fingerprinting algorithm approach.

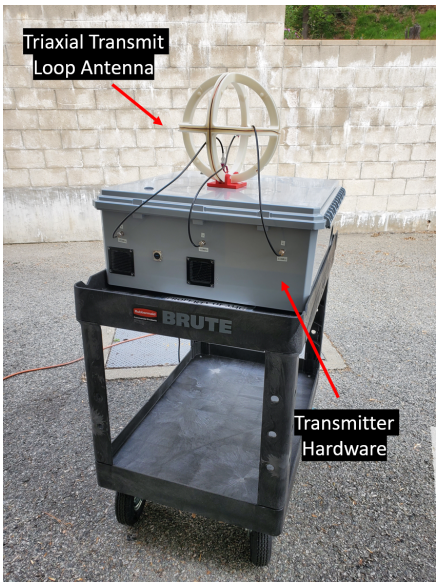
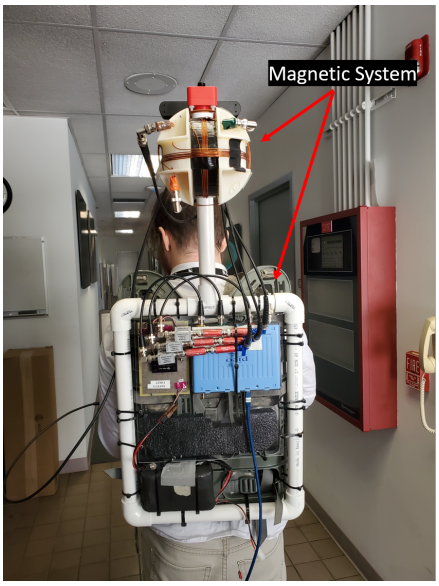
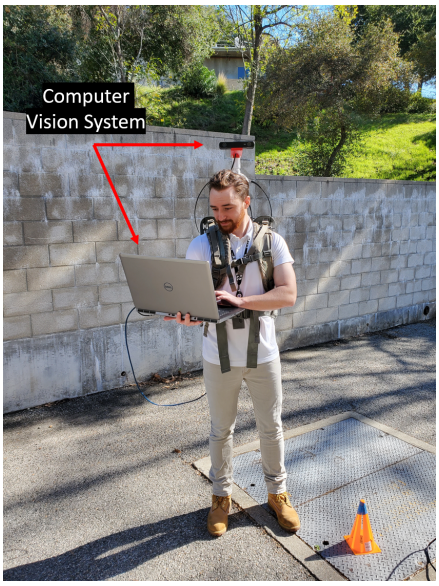


Figure 6.9: Mobile transmitter unit placed outside of building generating magnetic fields at 3 MHz for position-sensing.



(a) Magnetic prediction subsystem with triaxial loop antenna, filters, LNAs, and oscilloscope.



(b) Computer vision subsystem with stereoscopic camera.

Figure 6.10: Mobile receiver unit being used to perform real-time prediction of individual in steel-reinforced structure.

For this demonstration, a data collection program was developed that displays a demo screen GUI. This displays live video feed from our camera, received magnetic field power data versus time, and a screen the displays current position determined from the camera, past positions from the camera, and predicted position from the MQS system. The predicted position from the MQS system is presented as a red circle that overlaps the current position from the camera (shown as a blue dot). An image of our demo screen is shown in Fig. 6.11. What makes this demo special is that processing and data prediction is performed and displayed to the user in real-time, which differs from a post-processing approach used previously in the determination of our developed mathematical model.

A live walk-through of this system is shown in [52]. In this demonstration, a user walks through a steel-reinforced building, entering different parts of an office area. As the user navigates, it is shown that the current position is consistently and accurately predicted. It is seen that there is a slight latency in the processing of the MQS data compared to the computer vision data, which is indicated by the the red circle following the blue dot in the

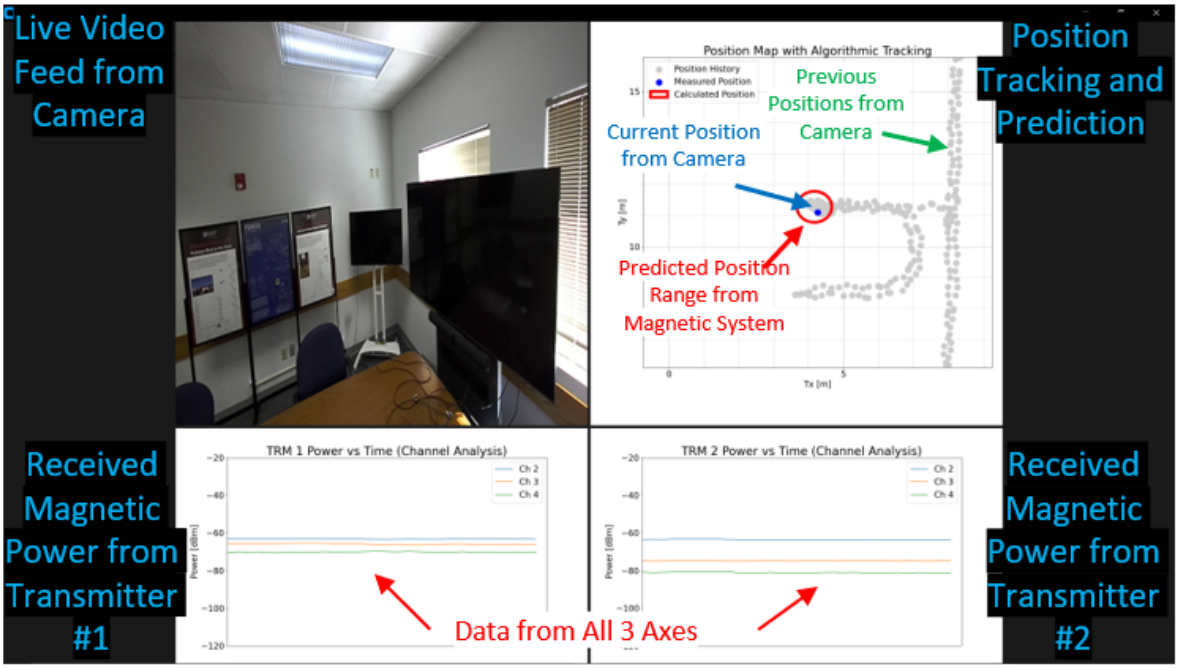


Figure 6.11: Position-sensing demo screen showing received magnetic field power, live video feed, and positioning prediction with calculated errors.

upper-right of the demo screen. This delay can be corrected with simple algorithms.

After walking through the building, the user then enters a room and blocks the stereoscopic camera from receiving light and predicting accurate positioning. This is done to simulate a blackout environment in which the field-of-view is completely obstructed. This is analogous to an environment in which there is heavy smoke that makes it impossible for emergency responders to see clearly. When this occurs, the user continues to walk around the room. The predicted position from the MQS system succeeds in predicting positioning within a small margin of error. For the majority of the demonstration, it is shown that the predicted position is within 1 meter of accuracy from the computer vision positioning, which is satisfactory for first responder applications.

6.5 Conclusion

The development of this multiaxial MQS sensor fusion system and the demonstration of its performance for position-sensing in real-time serve as the culmination of over one year of dedicated research. After diligently studying the radiation characteristics of $LiNbO_3$ transmitters, it was determined that a new system needed to be developed to provide sufficient signal coverage within a steel-reinforced structure. After designing the system architecture and developing portable transmitter and receiver hardware, we collected data and developed mathematical models that adequately predict magnetic power decay deep within the building. These models are insufficient at close range, however, which prompted a fingerprinting approach to be utilized during a live demonstration. During the live demonstration, it was shown that the MQS system predicts positioning within a 1 meter accuracy compared to positioning data determined from our computer vision subsystem. Despite resulting in a successful demonstration, there is much work to be done to extend this system to multi-story buildings. Additionally, there is work to be done regarding the miniaturization of receiver hardware to ensure a more compact and portable form-factor for emergency responders.

CHAPTER 7

Conclusion and Future Work

7.1 Recapitulation of Key Findings

Through this research, we have studied the radiation performance of $LiNbO_3$ piezoelectric transmitters for EQS field transmission, specifically for the application of position-sensing for first responders. We found that electric field generation is proportional to supplied excitation voltage, and that there is a linear regime of operation [3]. This is due to hysteresis effects inherent to the piezoelectric crystal which can result in the saturation and deterioration of the crystal. The extreme of pushing piezoelectric transmitters is that the crystal itself will break at the point of greatest strain [14]. We also confirmed the dipole-like field pattern of these devices by developing a novel method of pattern measurement that takes advantage of the reciprocal nature of their EQS radiation using large metal plates. Understanding the near field radiation patterns of these transmitters is paramount in ensuring consistent and predictable radiation.

After studying the radiation properties of these devices at LF and VLF, we extended operation to the high frequency (HF) range by developing a $LiNbO_3$ transmitter with resonant frequency of 1 MHz. To our knowledge, this is the first time radiation has been demonstrated with one of these devices. We found that our transmitter radiates electric fields with a predictable $1/r^3$ drop-off in a LoS environment. This device was calculated to have a radiation efficiency two orders of magnitude greater than that of a conventional dipole ESA. The extension of this technology opens many doors for further development not limited to position-sensing applications.

This work experienced a significant turning point when LoS measurements were obtained

in a steel-reinforced building with a $LiNbO_3$ transmitter radiating at 82 kHz. It was found that the EQS fields radiated by this device attenuated too quickly to be reliably used for position-sensing with adequate coverage of SNR within a structure of this type. This discovery prompted a change in system architecture in which it was determined to utilize a multiaxial MQS system centered at 3 MHz. The decision was made based on the reliability of MQS radiation as well as 3 MHz having a wavelength that is supported within the building, analogous to a certain mode being supported in a rectangular waveguide.

This discovery prompted the design of a multiaxial system architecture in which multiple transmitters radiate MQS fields outside of a steel-reinforced structure. These fields are then received by a mobile backpack unit with multiaxial MQS receiver integrated with computer vision location prediction. The hardware development and sensor fusion integration was presented, and a mathematical model was developed to predict positioning in a single-story structure. This work culminated in an online demonstration for the Department of Homeland Security Science and Technology Directorate in which the system was shown to accurately predict positioning even when the computer vision system fails. This functionality is critical for predicting the position of first responders in environments where field of view is significantly obstructed.

This work has extended the investigation of piezoelectric transmitters as well as developed an accurate and reliable position-sensing system for first responders. This presents many opportunities for further research in which this technology can be enhanced or utilized for alternate applications.

7.2 Extension of Piezoelectric Transmitter Operation

Prior to our investigation into the radiation characteristics of $LiNbO_3$ transmitters at 1 MHz, the open literature had been limited to studying devices resonant below 100 kHz [3, 14, 16, 26, 38–40]. In demonstrating that these devices still radiate electric fields in the HF regime, the door of application possibilities has been swung wide open. For example, arraying these devices on spacecraft could enhance radar and remote sensing applications,

utilizing HF radiation for deep penetration of Earth's surface and other planetary bodies. To pursue further research in this development, we propose investigation into integrating direct antenna modulation (DAM) as well as studying the arraying behavior of these transmitters.

7.2.1 Direct Antenna Modulation

DAM presents a novel approach to enhancing the capabilities of piezoelectric transmitters. It modifies the radiation properties of the device in real-time to encode data directly into transmitted signals, allowing for more complex modulation schemes to be employed without introducing physical or electrical complexity to the system [14, 53]. DAM's ability to dynamically change radiation patterns and frequencies significantly improves data throughput and radar system accuracy [54]. Incorporating DAM into piezoelectric transmitters can also improve system security, which can be critical in radar applications. By altering the transmitter's radiation characteristics, DAM can assist in shielding signals from eavesdropping and unauthorized tracking. Future work in the integration of DAM with piezoelectric transmitters could lead to more advanced system integration.

7.2.2 Piezoelectric Transmitter Arraying

Another method of extending this technology is to develop arrays of these devices. Some efforts have been made in the kHz regime to study the effect this has on radiation [26] but there is much work to be done at higher frequencies. The optimal spacing between elements to balance close proximity and gain trade-offs has yet to be determined. We believe that developing these into an array configuration could improve radiated field magnitude and steer-ability. Also, considering these devices are much smaller than conventional antennas at these frequencies, it would be ideal to decrease size, even when creating arrays of many elements. This, along with DAM, could develop and advance the technology for use in radar, tracking, and communications.

7.3 MQS System Scaling

Since we have shown that our MQS sensor fusion system succeeds in determining the position of individuals navigating within a single-story heavily steel-reinforced building, there are several paths to take in extending this system. One possible path is to extend the system to work in multi-story environments. This path focuses on extending the hardware and increasing the complexity of the positioning algorithm. Another path is toward the miniaturization of the receiver hardware, which would make the system much more portable and deployable for first responder applications. Both of these directions are highly favorable, and their integration could lead to a highly robust positioning system for first responders.

7.3.1 Positioning in Multi-Story Steel-Reinforced Structures

Some ongoing efforts for this project include extending its operation to multi-story buildings, with the goal of developing a system for high-rise infrastructure. This extension is vital for first responders, and needs to be highly accurate to ensure the safety and efficiency in performing emergency operations. This path requires a minimum of three transmitters to perform triangulation algorithms at the receiver, determining the position based on received magnetic power. This coordinate would then be sent at higher frequency to a base station that observes the incoming positional data. It would be ideal to also integrate a GNSS receiver that maps the relative coordinates of the MQS system to a global reference plane. The system also needs to be capable of providing reliable and accurate positioning within stairwells, which are the primary method of vertical ascent and descent in emergency environments.

7.3.2 Miniaturization of System Hardware

Efforts are ongoing to further miniaturize the electronics of both the transmitter and receiver. The size of the receiver electronics are of greatest concern, since the receiver will be carried by the emergency responder. These devices need to be small, portable, lightweight, and

rugged to ensure that they can be used reliably. This work includes decreasing the size of the multiaxial receiver loop antenna by decreasing the diameter and increasing the number of windings. Additionally, integrating filters and LNAs directly onto PCBs, rather than using larger components with BNC connectors, would enhance compactness and reliability. This would allow us to use surface mount technology that is much smaller and more compact. A slight architecture change is required for this method to transition from using a multi-port oscilloscope to using a single-port spectrum analyzer. This would require additional components, such as an RF switch and possibly mixers to downconvert the received signal tones. Ideally, combining miniaturized hardware with a well-developed triangulation network could improve the present system and assist in saving the lives of our first responders and other individuals in danger.

REFERENCES

[1] S Sherrit, H D Wiederick, B K Mukherjee, and M Sayer. An accurate equivalent circuit for the unloaded piezoelectric vibrator in the thickness mode. *Journal of Physics D: Applied Physics*, 30(16):2354–2363, Aug. 1997.

[2] R. S. Weis and T. K. Gaylord. Lithium niobate: Summary of physical properties and crystal structure. *Applied Physics A*, 37(4):191–203, 1985.

[3] Tristan A. Wilson, Stewart Sherrit, Srinivas Prasad Mysore Nagaraja, Brook Feyissa, Devin Willey, and Darmindra D. Arumugam. High drive voltage studies on lithium niobate length extensional resonators and their generated quasistatic electric fields. In *2023 IEEE International Ultrasonics Symposium (IUS)*, Sep. 2023.

[4] J.G. Smits. Iterative method for accurate determination of the real and imaginary parts of the materials coefficients of piezoelectric ceramics. *IEEE Transactions on Sonics and Ultrasonics*, 23(6):393–401, 1976.

[5] Department of Homeland Security. Pointer. `https://www.dhs.gov/science-and-technology/pointer`, 2021. Accessed: 2024-05-28.

[6] Jet Propulsion Laboratory. Pointer: Seeing through walls to help locate firefighters. `https://www.jpl.nasa.gov/news/pointer-seeing-through-walls-to-help-locate-firefighters`, 2021. Accessed: 2024-05-28.

[7] NASA Jet Propulsion Laboratory. Pointer: Nasa tech demonstrated in a simulated house fire. `https://www.youtube.com/watch?v=trM7Jue6T70`, 2021.

[8] Jack D. Bush, Darmindra D. Arumugam, and Brook Feyissa. Counter-wound normal-mode helical antenna as an electrically small electro-quasi-static exciter. *IEEE Antennas and Wireless Propagation Letters*, 19(2):287–291, Dec. 2019.

[9] Hermann A. Haus and James R. Melcher. *Electromagnetic Fields and Energy*, chapter 3, pages 3–27. Prentice Hall, 1989.

[10] Charles Kittel. *Introduction to Solid State Physics*. Wiley, Hoboken, NJ, 8th edition, 2004.

[11] Stefan Johann Rupitsch. *Piezoelectric Sensors and Actuators Fundamentals and Applications*, chapter 6. Springer-Verlag GmbH Germany, 2019.

[12] James A. Bickford, Ronald S. McNabb, Paul A. Ward, Daniel K. Freeman, and Marc S. Weinberg. Low frequency mechanical antennas: Electrically short transmitters from mechanically-actuated dielectrics. In *Proc. IEEE Int. Symp. Antennas Propag. USNC/URSI Nat. Radio Sci. Meeting*, pages 1475–1476, San Diego, CA, USA, Jul. 2017.

[13] L. J. Chu. Physical limitations of omni-directional antennas. *Journal of Applied Physics*, 19(12):1163–1175, Dec. 1948.

[14] Mark A. Kemp, Matt Franzi, Andy Haase, Erik Jongewaard, Matthew T. Whittaker, Michael Kirkpatrick, and Robert Sparr. A high q piezoelectric resonator as a portable vlf transmitter. *Nature Communications*, 10(1715), Apr. 2019.

[15] Srinivas Prasad M N, Rustu Umut Tok, Foad Fereidoony, Yuanxun Ethan Wang, Rui Zhu, Adam Propst, and Scott Bland. Magnetic pendulum arrays for efficient ulf transmission. *Scientific Reports*, 9(13220), Sep. 2019.

[16] A. E. Hassanien, M. Breen, M.-H. Li, and S. Gong. Acoustically driven electromagnetic radiating elements. *Scientific Reports*, 10(17006), Oct. 2020.

[17] A. W. Warner, M. Onoe, and G. A. Coquin. Determination of Elastic and Piezoelectric Constants for Crystals in Class (3m). *The Journal of the Acoustical Society of America*, 42(6):1223–1231, Jul. 2005.

[18] Don A. Berlincourt, Daniel R. Curran, and Hans Jaffe. 3 - piezoelectric and piezomagnetic materials and their function in transducers. In Warren P. Mason, editor, *Physical Acoustics*, pages 169–270. Academic Press, 1964.

[19] S. Sherrit, S.P. Leary, B.P. Dolgin, and Y. Bar-Cohen. Comparison of the mason and klm equivalent circuits for piezoelectric resonators in the thickness mode. In *1999 IEEE Ultrasonics Symposium. Proceedings. International Symposium*, volume 2, pages 921–926, 1999.

[20] Stewart Sherrit, Hyeong Jae Lee, Xiaoqi Bao, Mircea Badescu, and Yoseph Bar-Cohen. Composite piezoelectric resonator 1D modeling with loss. In Ryan L. Harne, editor, *Behavior and Mechanics of Multifunctional Materials IX*, volume 11377, pages 113770T1–113770T15. International Society for Optics and Photonics, SPIE, 2020.

[21] K.S. Van Dyke. The piezo-electric resonator and its equivalent network. *Proceedings of the Institute of Radio Engineers*, 16(6):742–764, 1928.

[22] Stewart Sherrit. *Losses, Dispersion and Field Dependence of Piezoelectric Materials*. Phd thesis, Queen's University, 1997. Appendix B4.

[23] Ieee standard on piezoelectricity. *IEEE Std. 1516-2000*, pages 1–74, 1988.

[24] R. Holland. Representation of dielectric, elastic, and piezoelectric losses by complex coefficients. *IEEE Transactions on Sonics and Ultrasonics*, 14(1):18–20, 1967.

[25] Skyler Selvin, M. N. Srinivas Prasad, Yikun Huang, and Ethan Wang. Spinning magnet antenna for vlf transmitting. In *Proc. IEEE Int. Symp. Antennas Propag. USNC/URSI Nat. Radio Sci. Meeting*, pages 1477–1478, San Diego, CA, USA, Jul. 2017.

[26] Zhaodong Gao, Ming Su, Yuanan Liu, Meng Zhang, Chuming Yan, Jing Hao, Jifeng Lv, Xilian Chen, and Zihan Lin. Field-based circuit model of acoustically actuated piezoelectric antenna for characteristic evaluation and array applications. *IEEE Transactions on Antennas and Propagation*, 70(12), Dec. 2022.

[27] Motohisa Kanda and David Orr. Generation of standard electromagnetic fields in a tem cell. Technical report, National Bureau of Standards, Aug. 1988.

[28] B. E. Roseberry and R. B. Schulz. A parallel-strip line for testing rf susceptibility. *IEEE Transactions on Electromagnetic Compatibility*, 7(2):142–150, 1965.

[29] Arthur H Firester. Design of square helmholtz coil systems. *Review of Scientific Instruments*, 37(9):1264–1265, 1966.

[30] Muhammad Saqib, SN Francis, and JN Francis. Design and development of helmholtz coils for magnetic field. In *2020 International Youth Conference on Radio Electronics, Electrical and Power Engineering (REEPE)*, pages 1–5. IEEE, 2020.

[31] E.G.Lambert. Measurement of electric and magnetic fields from alternating current power lines. *IEEE Transactions on Power Apparatus and Systems*, (4):1104–1114, 1978.

[32] Andres F Restrepo Alvarez, Edinson Franco-Mejia, and Carlos R Pinedo-Jaramillo. Study and analysis of magnetic field homogeneity of square and circular helmholtz coil pairs: A taylor series approximation. In *2012 VI Andean Region International Conference*, pages 77–80. IEEE, 2012.

[33] H Michael Gach, Austen N Curcuru, Sasa Mutic, and Taeho Kim. B0 field homogeneity recommendations, specifications, and measurement units for mri in radiation therapy. *Medical physics*, 47(9):4101–4114, 2020.

[34] R. Jordan et al. The mars express marsis sounder instrument. *Planetary and Space Science*, 57(14):1975–1986, 2009.

[35] K. Fujimoto and H. Morishita. *Modern Small Antennas*. Modern Small Antennas. Cambridge University Press, 2013.

[36] Essam Heggy et al. Airborne sounding radar for desert subsurface exploration of aquifers: Desert-sea: Mission concept study [space agencies]. *IEEE Geoscience and Remote Sensing Magazine*, 12(1):162–185, 2024.

[37] Robert M. Beauchamp et al. Can airborne ground penetrating radars explore groundwater in hyper-arid regions? *IEEE Access*, 6:27736–27759, 2018.

[38] Ahmed E. Hassanien, Michael Breen, Ming-Huang Li, and Songbin Gong. A theoretical study of acoustically driven antennas. *Journal of Applied Physics*, 127(1), Jan. 2020.

[39] Srinivas Prasad Mysore Nagaraja, Brook Feyissa, Tristan A. Wilson, Jack Bush, and Darmindra D. Arumugam. Electric field pattern measurements of acoustically driven piezoelectric field emitters. In *2023 Antenna Measurement Techniques Association Symposium (AMTA)*, Oct. 2023.

[40] Zhaodong Gao, Ming Su, Yuanan Liu, Chuming Yan, and Xilian Chen. Metal-loaded acoustically actuated piezoelectric antenna and its radiation efficiency limit. *IEEE Transactions on Antennas and Propagation*, 71(5):3938–3949, Mar. 2023.

[41] Stewart Sherrit and Binu K Mukherjee. Characterization of piezoelectric materials for transducers. *arXiv preprint arXiv:0711.2657*, 2007.

[42] J. S. McLean. A re-examination of the fundamental limits on the radiation q of electrically small antennas. *IEEE Transactions on Antennas and Propagation*, 44(5):672–, May 1996.

[43] Valter Pasku, Alessio De Angelis, Guido De Angelis, Darmindra D. Arumugam, Marco Dionigi, Paolo Carbone, Antonio Moschitta, and David S. Ricketts. Magnetic field-based positioning systems. *IEEE Communications Surveys Tutorials*, 19(3):2003–2017, Mar. 2017.

[44] Y. Zheng, Q. Li, X. Wang, C. Wang, L. Wu, and X. Li. Advanced positioning system for harsh environments using time-varying magnetic field. *IEEE Transactions on Magnetics*, 57(6):1–12, Jun. 2021.

[45] Valter Pasku, Alessio De Angelis, Marco Dionigi, Guido De Angelis, Antonio Moschitta, and Paolo Carbone. A positioning system based on low-frequency magnetic fields. *IEEE Transactions on Industrial Electronics*, 63(4):2457–2468, Apr. 2016.

[46] Valter Pasku, Alessio De Angelis, Guido De Angelis, Antonio Moschitta, and Paolo Carbone. Magnetic field analysis for 3-d positioning applications. *IEEE Transactions on Instrumentation and Measurement*, 66(5):935–943, May 2017.

[47] Guanglie Ouyang and Karim Abed-Meraim. A survey of magnetic-field-based indoor localization. *Electronics*, 11(6), Mar. 2022.

[48] Darmindra D. Arumugam. Through-the-wall magnetoquasistatic ranging. *IEEE Antennas and Wireless Propagation Letters*, 16:1439–1442, Dec. 2017.

[49] Darmindra D. Arumugam, Joshua D. Griffin, Daniel D. Stancil, and David S. Ricketts. Three-dimensional position and orientation measurements using magneto-quasistatic fields and complex image theory [measurements corner]. *IEEE Antennas and Propagation Magazine*, 56(1):160–173, Feb. 2014.

[50] Darmindra D. Arumugam. Single-anchor 2-d magnetoquasistatic position sensing for short to long ranges above ground. *IEEE Antennas and Wireless Propagation Letters*, 15:1325–1328, Dec. 2016.

[51] Yuanxun Zheng, Qinghua Li, Changhong Wang, Xinnian Li, and Baisheng Yang. A magnetic-based indoor positioning method on fingerprint and confidence evaluation. *IEEE Sensors Journal*, 21(5):5932–5943, 2021.

[52] Tristan Wilson. Pointer version 2, demo 1. `https://youtu.be/_XXzQfkQza8`, 2024. Accessed: June 2, 2024.

[53] Antonio Raffo, Francesco Crupi, and Salvatore Costanzo. *Software defined radar for monitoring and sensing applications*. PhD thesis, University of Calabria, 2018.

[54] Lothar Reindl, Christian C. W. Ruppel, and Stephan Berek. Design, fabrication, and application of precise saw delay lines used in an fmcw radar system. *IEEE Transactions on Microwave Theory and Techniques*, 2001.